

# Optimal Time Lags from Causal Prediction Model Help Stratify and Forecast Nervous System Pathology

**Theodoros Bermpferidis**

Rutgers, The State University of New Jersey

**Richa Rai**

Rutgers, The State University of New Jersey

**Jihye Ryu**

University of California, Los Angeles

**Elizabeth Torres** (✉ [ebtorres@psych.rutgers.edu](mailto:ebtorres@psych.rutgers.edu))

Rutgers, The State University of New Jersey

---

## Research Article

**Keywords:** Granger causality, stochastic analysis, gait, network connectivity, Parkinson's disease, healthy aging, FMR1 premutation carriers

**Posted Date:** March 6th, 2021

**DOI:** <https://doi.org/10.21203/rs.3.rs-279520/v1>

**License:**  This work is licensed under a Creative Commons Attribution 4.0 International License.

[Read Full License](#)

---

# Optimal Time Lags from Causal Prediction Model Help Stratify and Forecast Nervous System Pathology

Theodoros Bermpferidis<sup>1\*</sup>, Richa Rai<sup>1</sup>, Jihye Ryu<sup>4</sup> and Elizabeth B Torres<sup>1,2,3,\*</sup>

<sup>1</sup> Rutgers University, Psychology Department; tb642@psych.rutgers.edu

<sup>1</sup> Rutgers University, Psychology Department; rr708@psych.rutgers.edu

<sup>2</sup> Rutgers University Center for Cognitive Science (RUCCS); ebtorres@psych.rutgers.edu

<sup>3</sup> Computational Biomedicine Imaging and Modelling

<sup>4</sup> University of California Los Angeles, Neurosurgery Department; jihyeryu@mednet.ucla.edu

\* Correspondence: ebtorres@psych.rutgers.edu; Tel.: +011-732-208-3158 (E.B.T.)

Received: date; Accepted: date; Published: date

## Abstract

Traditional clinical approaches diagnose disorders of the nervous system using standardized observational criteria. Although aiming for homogeneity of symptoms, this method often results in highly heterogeneous disorders. A standing question thus is how to automatically stratify a given random cohort of the population, such that treatment can be better tailored to each cluster's symptoms, and severity of any given group forecasted to provide neuroprotective therapies. In this work we introduce new methods to automatically stratify a random cohort of the population composed of healthy controls of different ages and patients with different disorders of the nervous systems. Using a simple walking task and measuring micro-fluctuations in their biorhythmic motions, we show that gait is compromised in healthy aging and that in young FMR1 premutation carriers, gait forecasts, even by 15 years ahead, symptoms resembling those of elderly with Parkinson's disease. Our methods combine non-linear causal network connectivity analyses in the temporal and frequency domains with stochastic mapping, defining a new type of internal motor timings amenable to create personalized clinical interventions. We frame our results using the principle of reafference and operationalize them using causal prediction, thus renovating the theory of internal models for the study of neuromotor control.

**Keywords:** Granger causality; stochastic analysis; gait; network connectivity; Parkinson's disease; healthy aging; FMR1 premutation carriers

---

### 33 Introduction

34 Patients with Fragile-X Tremor Ataxia syndrome (FXTAS), patients with Parkinson's Disease  
35 (PPD) and patients in the broad spectrum of Autism (ASD) my all have motor issues detectable and  
36 tractable through gait patterns at different stages of their lifespan [1-10](#). Generally, these disorders share  
37 some common genes [11-13](#), but their phenotypic features differ depending on the person's age and on  
38 the evolution of various epigenetic factors [14,15](#). While the autistic patient may arrive at the diagnosis  
39 via Psychiatric/Psychological measures, devoid of motor criteria, it is highly probable that the PPD  
40 will do so through motor criteria from a movement disorders specialist in Neurology. In contrast, the  
41 FXTAS patient may receive an ASD diagnosis during childhood, when differences in communication  
42 and social interactions gain priority over motor issues [16,17](#) but then, later in life, as motor issues are  
43 exacerbated, they may gain the diagnosis of PPD. FMR1-premutation carriers may be considered  
44 neurotypical until later in adult life, when tremor, ataxia, and symptoms of parkinsonism become  
45 highly visible [18,19](#). Indeed, the FMR1 CGG repeat length predicts motor dysfunction [20](#) of the type that  
46 PPD have much later in life.

47 We know that motor activity reveals that aging with Autism greatly departs from typical aging  
48 [21](#) despite whether the person is or is not on psychotropic medications [22](#). We are also aware that  
49 parkinsonism, typically associated with human aging [3,23](#), is prevalent in Autistic adults [24](#). Indeed,  
50 the rate of parkinsonism in the general population aged 65–70 has been estimated at 0.9 % [23](#),  
51 compared to 20 % in ASD aged after 39 [24](#), when excess involuntary motions at rest have been  
52 quantified [21,25](#).

53 Parkinsonism in FMR1-premutation carriers may be indistinguishable from PD [26](#). And Fragile-  
54 X syndrome (FXS) has high penetrance in Autism [27](#) with genetic overlap across Parkinson, Ataxias,  
55 ASD and FXTAS [11](#). This points to a common pool of genes affecting both neurodevelopment and  
56 neurodegeneration, perhaps providing a new path to pre-emptively offer neuroprotective motor-  
57 sensory-based accommodations in early neurodevelopment gone astray [11](#). Given the high  
58 heterogeneity in their manifestations and the asynchronous nature of their developing severities,  
59 how could we automatically stratify a random draw of the population containing a mixture of these  
60 disorders?

61 Gait studies integrated with wearable sensors in natural activities have been very useful to  
62 ascertain various aspects of these phenotypes [19,28-30](#), but population statistics employed in these  
63 analyses are not personalized. They primarily focus on descriptive summary statistics from a priori  
64 assumed distributions, a procedure that incurs in loss of gross data [31](#). Further, owing to anatomical  
65 disparities confounding gait parameters, we need scaling methods that standardize outcomes and  
66 provide proper similarity metrics to compare across different subtypes of a given disorder. There is  
67 room to examine individual motor fluctuations within the context of dynamic network analyses and  
68 causal prediction [32](#). Here we integrate causal and non-causal network connectivity analytics to  
69 examine self-emergent patterns from standardized micro-movement spikes derived from gait-  
70 kinematics. We discuss our results within a new unifying framework to study disorders of the  
71 nervous systems across different diagnoses of disparate clinical criteria and yet, converging  
72 functional phenotypes.

### 73 Results

74 Granger causality (GC) is a mathematical concept that allows us to quantify the causal effect of  
75 a stochastic process A on a second stochastic process B. It compares the prediction error of a dynamic  
76 model that predicts the evolution of B without the presence of A with the error of a prediction model  
77 that includes both A and B. If the inclusion of A improves the prediction, we say that A causally  
78 predicts B ( $A \rightarrow B$ ) and we can assess the degree to which this is determined by the method of choice.  
79 Our approach to modeling and calculating the Granger causality assumes models with a single  
80 internal delay. This allows us to find, within a particular range, the internal delay that maximizes the  
81 causality from A to B. To implement our methods using time series data from a grid of 23 sensors  
82 collecting bodily orientations as the person walks, we first extract the angular speed time series  
83 (rad/s) over the span of 3-min walks. We then, build a data type that we have created the micro-

84 movements spikes (MMS [33](#)) which extracts the moment-to-moment fluctuations in the signal's  
85 amplitude provided by the peaks, and the fluctuations in inter-peak interval timings. This data  
86 derived from the sensors is unitless as it is standardized to characterize the dynamic behavior of  
87 motion by scaling out anatomical differences. This standardization of the data also enables us to  
88 compare the stochastic signatures of these participants' motions across a random draw of the  
89 population, while considering different ages and different clinical genotypes and phenotypes. As we  
90 keep the indexes into the original physical unit ranges, we can further estimate cross-population  
91 scales and boundaries for each parameter of interest.

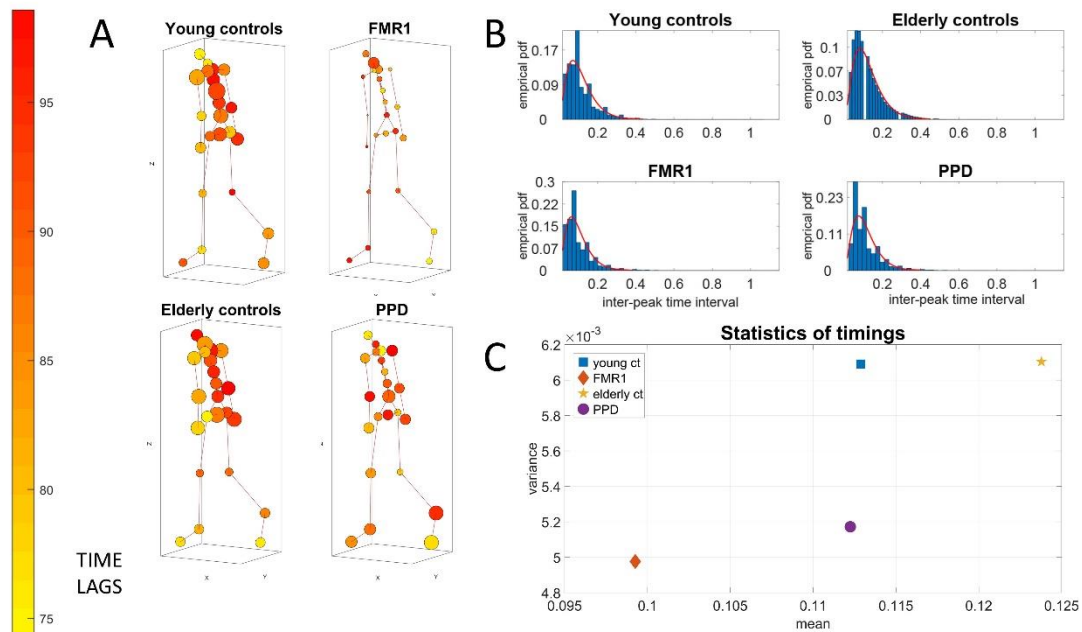
92 Upon standardization, we apply our technique between each directed pair of MMS time series  
93 across all 23 nodes corresponding to different joints across the full body. The maximum outwards  
94 GC of each node towards the rest of the body for the average GC-directed network of each group  
95 revealed marked differences from group to group. Furthermore, the average Optimal Lag network  
96 of maximum lags from a node to the rest of the body, assuming that the MMS series of that node, is  
97 the causal stochastic process, also revealed fundamental differences on timing across the different  
98 ages and nervous systems' disorders. We detailed them below:

#### 99 *Granger-Causal Networks Reveal Age-Dependent Gait Differences in Typical Controls*

100 As age increases in healthy participants, we see fundamental differences emerge in the patterns  
101 of GC prediction between their upper and lower body. The relative causal connectivity between  
102 upper to lower body is higher in elderly participants than in young controls. This can be appreciated  
103 in Figure 1A using an anthropomorphic interconnected network representation of the full body using  
104 the 23 nodes. The size of the node is proportional to the GC out degree value of that node as it  
105 connects to all other nodes. Furthermore, elderly control participants have in general lower optimal  
106 lag times of the lower extremities ( $p=0.0293$ ,  $t$ -test) suggesting an overall slowdown in information  
107 transmission and feedback between upper and lower extremities. Often, patterns such as  
108 bradykinesia and loss of gait control in pathologies of the nervous system are shown. Yet, here we  
109 observe them as a part of the natural aging process in this cross-sectional cohort of healthy controls.  
110 We use a colormap representation to indicate the lag values in Figure 1A, whereas in Figure 1B, we  
111 provide the empirical frequency histograms of the interpeak interval timings of the MMS. The  
112 corresponding physical times expressed in seconds distribute according to the continuous Gamma  
113 family of probability distributions, optimally fit to the empirical data, in a maximum likelihood  
114 estimation (MLE) sense. These patterns are depicted for the healthy controls in Figure 1B (top panels.)

#### 115 *FMR1-Carriers are Different from Controls of Comparable Age and from PPD*

116 Premutation carriers of the FMR1 gene show a significant decrease in GC connectivity across the  
117 body in relation to the young controls of comparable age ( $p=0.0061$ ;  $t$ -test) This is depicted in Figure  
118 1A along with fundamental differences in the patterns of optimal lags, which are abnormally lower  
119 than controls ( $p=2.7160e-04$ ;  $t$ -test). This reduction in optimal lag values in the premutation carriers is  
120 accompanied by a reduction in their timing variability that resembles (and perhaps forecasts) the  
121 type of reduction in variability observed in the PPD. The latter shows a significant reduction in GC  
122 across the body relative to the elderly controls ( $p=0.0021$ ;  $t$ -test). This is particularly the case in the  
123 torso, with lower lags in the lower body, when we compare them to the elderly controls. Figure 1C  
124 summarizes the statistics of the timing. This parameter space reveals healthy patterns of timing  
125 variability in the controls *vs.* atypically lower variability patterns in the premutation carriers and the  
126 PPD.



127

128

129

130

131

132

133

134

135

136

137

Figure 1: **GC Optimal Lag Maps and timing information.** Anthropomorphic network representation of human walking patterns. The nodes' size is proportional to the number of outgoing links connected to the other nodes in the network (out degree) of the average GC network. The color of the nodes is the maximum optimal lag response of a node with the rest of the body for the average Lag Response network. A unit of one lag refers to the distance in time between two peaks. The actual physical time between the two peaks can vary. The frequency histograms depict the distribution of the inter-peak timings for each group. The empirical distributions are well fitted by the gamma family of distributions. For the young controls, the average inter-peak timing is 0.1129 seconds with a std of 0.0780. For the elderly controls, 0.1238 with a std of 0.0781. For the FMR1 carriers, 0.0993 with a std of 0.0705. For the PPDs, 0.1122 with a std of 0.0719.

138

*Prevalence of causal feedback loops is much higher in controls groups*

139

140

141

142

143

144

145

146

147

148

149

150

151

152

153

154

155

156

157

158

159

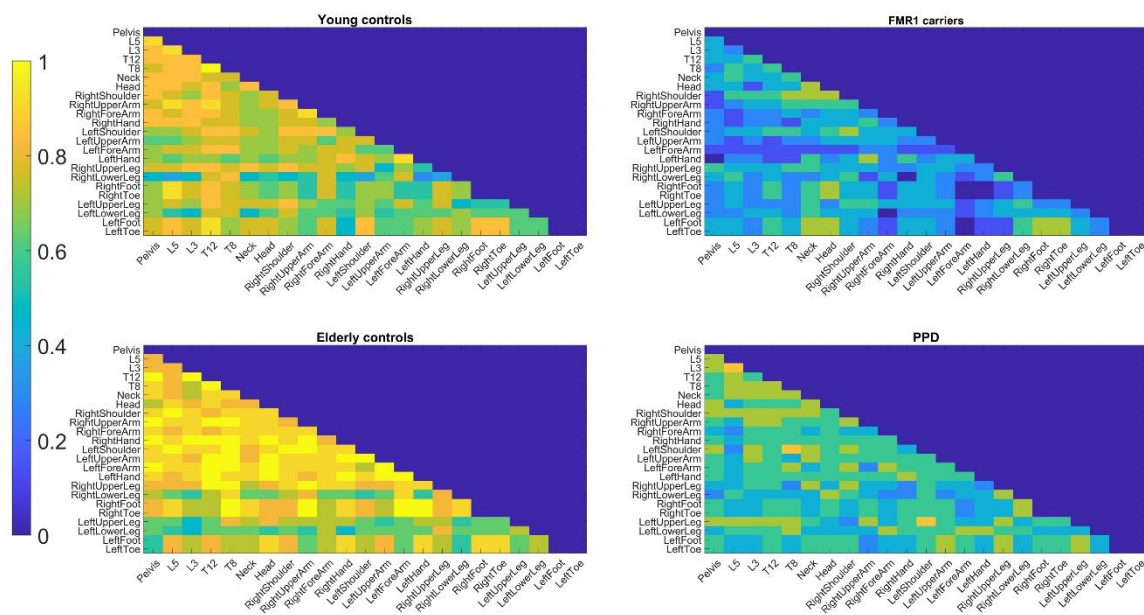
160

An important concept in the theory of neuromotor control, first introduced by von Holst and Mittelstaedt in 1950, is known as the principle of reafference <sup>34</sup>. Every time a motor movement is to be initiated, a motor signal is sent to the periphery to perform a certain movement through the efferent nerves, which is called efference. Similarly, the sensory input coming from the periphery towards the Central Nervous System (CNS) is called afference. The afference consists of two components. The first component is called exo-afference and is the afferent input generated from the environment. The second component is called endo-afference, which is the sensory input self-generated from the body's own actions. We discovered that during complex actions, the endo-afference is separable into intended segments (under voluntary control), and incidental segments (occurring spontaneously and largely beneath awareness <sup>35</sup>.) Because of its internal origins and its relation to movements, the latter is known as kinesthetic reafference, though it also includes pain and temperature afference from the corresponding fibers at the periphery. According to the principle of reafference, every time a movement is initiated by sending information to the motor system, a copy of the signal is created, called the efferent copy or corollary discharge, and is sent to the CNS to inform of the impending movement. This enables the CNS to distinguish sensory signals stemming from external environmental factors, from sensory signals coming from the body's own actions. The efference copy is provided as input to a forward internal model to predict the sensory consequences of the motor action to be initiated. Comparing the predicted movement with the actual movement is precisely what allows the CNS to recognize its own actions and at a higher cognitive level, form a sense of self. In the internal models of neuromotor control, the intended consequences from voluntary acts can be evaluated using the principle of reafference <sup>36,37</sup>. A non-trivial extension of this idea is to include, in addition to consequences from voluntary actions, the unintended consequences from

161 those incidental actions that occur spontaneously, without instructions or precise targets. This idea  
 162 has been proposed and investigated by our group, to define different levels of volition [35,38-40](#), and  
 163 proposed as a fundamental ingredient of the more general concept of motor agency.

164 The principle of refference has been a source of inspiration for decades in biology, cognitive  
 165 science, vision, neuromotor control and robotics, and attempts to model it fall usually within the  
 166 realm of control theory and dynamical systems [41-44](#). Our approach to operationalize this principle  
 167 does not assume a particular deterministic feedforward model. It rather assumes stochastic dynamic  
 168 models for each body node and for pairs of body nodes. If the principle of refference implies the  
 169 presence of feedback loops between the CNS and the periphery, the fact that information is carried  
 170 along efferent and afferent pathways and processed in various organs of the CNS (e.g. the cerebellum  
 171 [36](#)) implies that it is not an instantaneous process, but it is characterized by some internal timing. In  
 172 fact, timing is important to accurately predict the consequences of one's actions, coordinating such  
 173 actions in space and time. Timing plays a central role in agency, leading to a sense of action ownership  
 174 and self-awareness. Hence, the causal analytics, being sensitive to the choice of timing of the model,  
 175 can be used to estimate the actual motor timings in the nervous system.

176 But how exactly can we detect the presence or not of a feedback loop between two nodes? Once  
 177 again, the answer can be found in one of Granger's definitions in his original paper [45](#). Following the  
 178 formal definition of causality, he proceeds to define feedback. According to the definition, if A and B  
 179 are two stochastic processes, and A causes B in the Granger sense, but also B causes A in the Granger  
 180 sense, *i.e.*, causality occurs in both directions, then that implies the presence of a feedback loop  
 181 between the two processes. Then, simply checking for each undirected pair of body nodes, we can  
 182 check whether the causal connectivity graph that we derived earlier exhibits causality in both  
 183 directions. Then, we can determine whether there is a feedback loop between the nodes, within the  
 184 accuracy of our model and the choice of timing.



185  
 186 **Figure 2: Feedback loops differ across groups.** For each group, the figures show the percentage of  
 187 subjects within the group for whom a feedback loop was detected between each pair of body nodes.

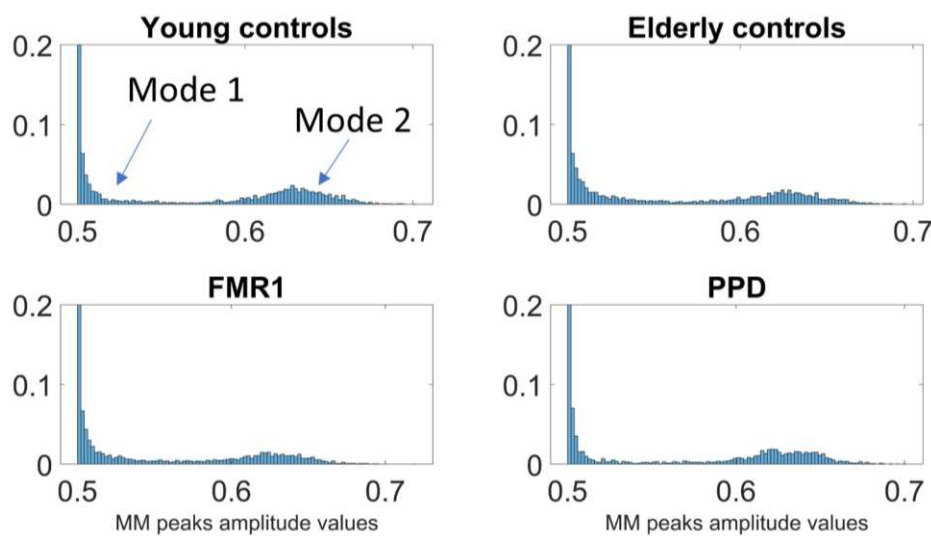
188 Addressing Granger's notion of feedback (up to our limited assumption of an autoregressive  
 189 model explained in the Materials and Methods Figure 14) provides the results depicted in Figure 2.  
 190 Once again, the healthy controls show (cross sectionally) the effect of natural aging on the feedback  
 191 patterns that we take pairwise across these 23 nodes of the body. Consistent with the Figure 1A  
 192 summarizing the group patterns (in one direction  $A \rightarrow B$ ), we see the patterns of feedback loops across  
 193 each group, detected when including  $B \rightarrow A$  and obtaining GC in both directions. Young healthy  
 194 controls have a more distributed pattern across the body, in contrast to elderly controls, who show a

195 diminished pattern in the lower extremities accompanied by an abnormally higher feedback-loop  
 196 pattern across the upper extremities, perhaps compensating for their lacking in the lower extremities.  
 197 This decrease in feedback loops generalizes across all bodily nodes in PPD, but interestingly, the  
 198 decrease is even more evident in the FMR1 premutation carriers, closer in age to the healthy young  
 199 controls. At such a young age compared to the PPD, these patterns in the FMR1 premutation carriers  
 200 forecast trouble on the horizon, of the type that elderly PPD eventually show.

### 201 *Identification of Different Groups' Subtypes*

202 One of the current challenges in data-driven analyses is to automatically identify self-emerging  
 203 subtypes of a disorder on a spectrum, as patterns stratify to form clusters of data points across a given  
 204 scatter. We here address this automatic stratification of a random draw of the population composed  
 205 of different types of patients and ages using various parameter spaces derived from the stochastic  
 206 patterns of the gross data that is often thrown away or smoothed out through grand averaging.

207 For each participant, we calculated the trajectory of the Center of Mass of the lower body in 3D  
 208 space and we extracted the MMS series from the Euclidean norm of the position time series. Upon  
 209 obtaining the standardized (scaled) speed amplitudes, we obtained the peaks and calculated the  
 210 empirical distributions of the inter-peak-interval timings of these MMS series. We noted the presence  
 211 of multiple modes in the frequency histograms and performed the Hartigan Dip test of unimodality  
 212 [46](#). We performed this statistical test both on the patterns from each participant separately and pooling  
 213 the data across participants for each group. For the latter, we did so after concatenating the MMS  
 214 series data of all subjects within a group. The Hartigan Dip Unimodality test per group showed that  
 215 for all groups the total empirical distributions fail the unimodality test. All groups distributed  
 216 bimodally, yet how the modes grouped had specific patterns particular to each group. This is  
 217 depicted in Figure 3.  
 218

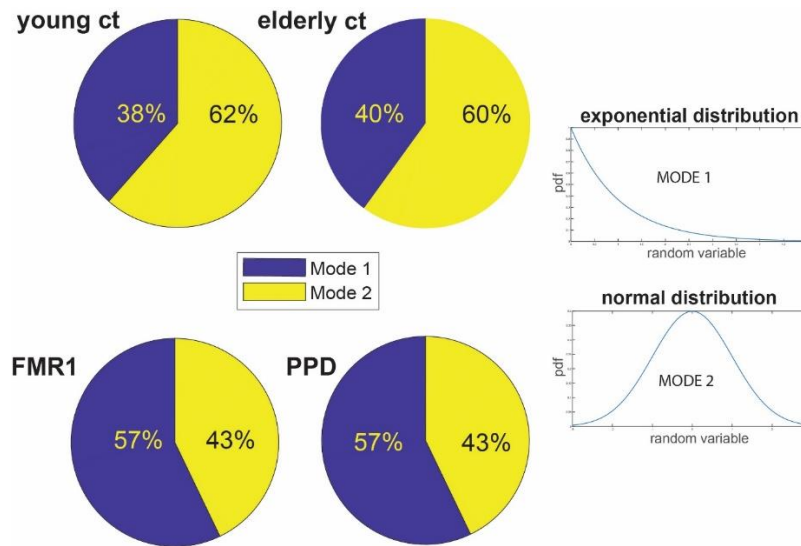


219

220 **Figure 3: Non-unimodal distributions of MMS from peak angular speed amplitudes differentiate**  
 221 **groups.** Different modes are specific to each cohort, mode 1 exponential and mode 2 Gaussian, with  
 222 different dispersions and percentages of points in each mode.

223 The first mode with lower values of the standardized MMS peaks amplitude was well fit by an  
 224 exponential distribution, whereas the second mode was well fit by a Gaussian distribution that had  
 225 the lowest dispersion in healthy young controls. In elderly controls, the percentage of points in the  
 226 exponential mode increased, and so did in FMR1 premutation carriers (closer in age to the young  
 227 controls) and the PPD, with the latter showing distribution patterns comparable to the carriers. To  
 228 see this, for each participant, we found in which mode the MMS activity was highest and calculated  
 229 the percentages of participants per group with the highest activity in each mode. Most young and

230 elderly controls have the highest MMS activity in the Gaussian mode. FMR1 carriers and PPDs have  
 231 higher prevalence of activity in the exponential mode (Figure 4.)  
 232

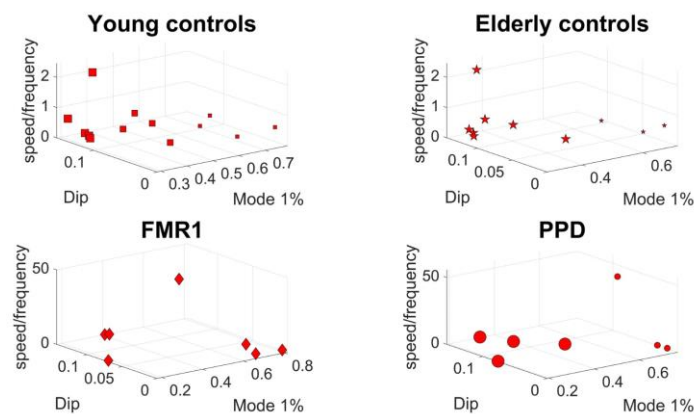


233

234 Figure 4: **Percentages of distribution's modes varies across groups** with lowest Exponential mode in  
 235 young controls and highest in FMR1 carriers and PPD. Gaussian mode is highest in young controls  
 236 and elderly controls and comparable between PPD (higher) and FMR1-carriers.

237 These patterns motivated a parameter space whereby we represent points as triplets -points in  
 238 a three-dimensional space, with coordinates representing the % of Mode 1 (exponential), the Dip  
 239 value from the Hartigan's Dip Unimodality test, and a scalar, giving the speed to frequency ratio (we  
 240 discuss below the motivation for using this ratio.) We then performed k-means clustering analyses  
 241 on the scatter of points from each group, to identify potential subtypes of activity in each cohort of  
 242 participants.

243 Figure 5 depicts the results (under the Euclidean distance metric; note that using the first mode  
 244 in this representation is sufficient, as the second mode percentages are complementary, *i.e.*, the sum  
 245 of percentages add to unit). Here the young controls have 3 clusters, and the other groups show 2  
 246 clusters (represented proportional to the size of the marker.)  
 247



248

249 **Figure 5: Subgroups within each group revealed by group's clusters.** The clusters for each group  
 250 using the k-means clustering algorithm with 3 for young controls and 2 for each of the other groups.  
 251 Subtypes of activity emerge for all groups. The empirical distributions for the MMS of the norm of  
 252 the lower body COM 3D position data series for the 4 groups are bimodal for all 4 groups.

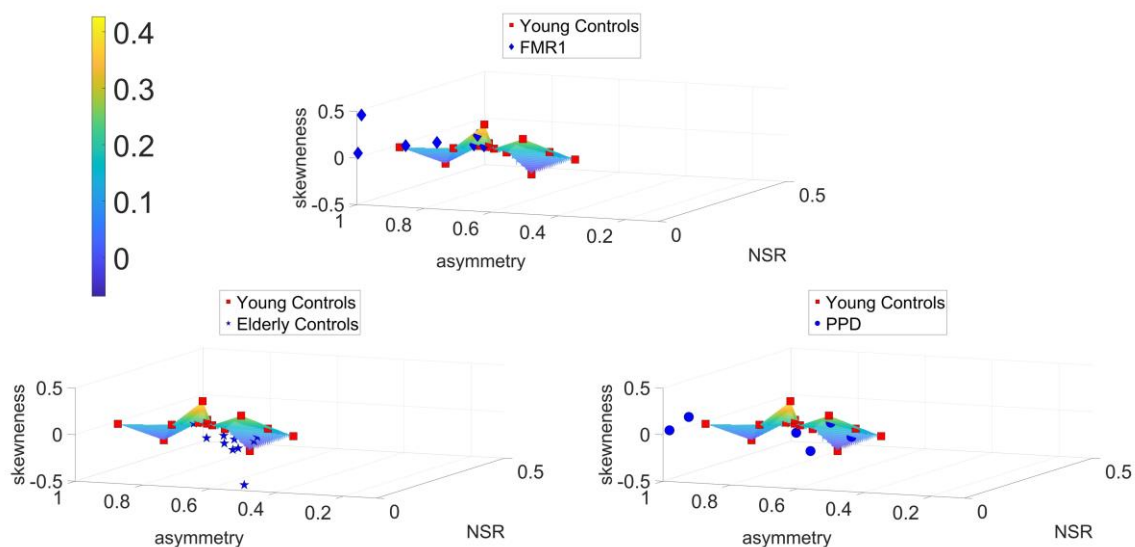
253 We identified 3 sub-types for the young controls group and 2 sub-types for the elderly controls.  
 254 There is a clear negative correlation between higher dips and lower first mode activity. The FMR1

255 carrier group has two subtypes. The first subtype has high first mode activity and low dip and the  
 256 second subtype has low first mode activity and high dip. A similar subtyping pattern is observed for  
 257 the PD group. The results can be appreciated in Figure 5, where the size of the marker denotes the  
 258 group within each cohort.

### 259 *Groups Differ Relative to Young Controls within a Parameter Space from the Data Stochastic Features*

260 The above results motivated us to quantify the departure of each group from the young controls  
 261 (as an ideal, normative state of motor control.) To that end, since the lower body and the pelvis play  
 262 a crucial role in gait control, we first characterized the patterns of fluctuation in the motions of the  
 263 pelvic area and upper leg nodes) by fitting the continuous Gamma family of probability distributions  
 264 as the optimal family in an MLE sense. Through this process, we obtained the scale parameter, which  
 265 is also the noise to signal ratio (NSR.) We obtained the average NSR and computed skewness of the  
 266 MMS series of the pelvic area for each subject. We also obtained the GC network asymmetry for each  
 267 subject (See Methods). This parameter space is shown in Figure 6 across all three comparisons. Two  
 268 sample *t*-tests, showed that young controls differ from elderly controls in mean skewness (with  
 269 borderline significance,  $p$ -value=0.096 , confidence interval=[0.0465, 0.0299] ). They also differ from  
 270 PPDs, significantly at the 0.05 alpha level, in mean pelvic NSR ( $p$ -value=0.0193 , confidence interval=[-  
 271 0.047, -0.00047187]). Finally, they differ significantly from FMR1 carriers in asymmetry ( $p$ -value=0.0107,  
 272 confidence interval=[-0.3386, -0.051]). In each plot, we fitted surfaces over the data samples for the  
 273 young controls to help visualize the differences and localize each cluster shifting across the parameter  
 274 space relative to this normative surface.

275 Notice in Figure 6 that FMR1 and PPD depart similarly from the normative surface of young  
 276 controls, while the elderly controls occupy a different location in this parameter space.



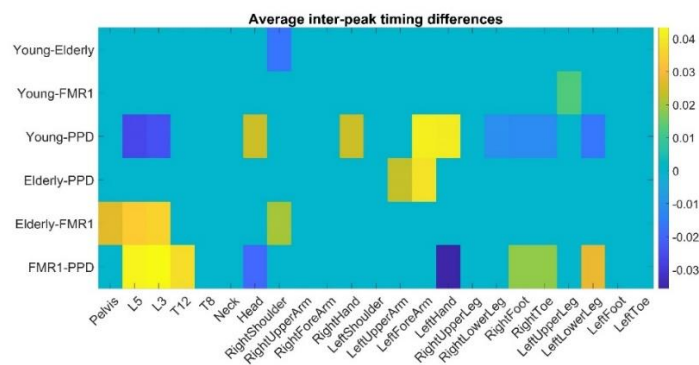
277

278 **Figure 6: Parameter space reveal differences across groups.** NSR, GC network asymmetry and  
 279 average Skewness are used to build a parameter space showing departure from young controls scatter  
 280 fitted by a surface. Scatters from the FMR1 carriers, the elderly controls and the PPD largely depart  
 281 from young controls' surface. Color bar reflects skewness range of values.

282 To examine temporal information within the efference-reafference framework, we calculated for  
 283 each undirected pair of angular speed MMS time series (*i.e.*, the full time series, not only the peaks)  
 284 the coupling frequency for which the cross-coherence is maximized. To that end, we found the  
 285 average of all cross-coherence outputs of a node's MMS series with all the other MMS series nodes in

286 the network (see Supplementary Materials). The time between two MMS is essentially a form of inter-  
 287 spike interval timing for the information flow crossing each body node. Therefore, we average for  
 288 each group the inter-spike times of each node and compare the rate of putative afferent (incoming)  
 289 and efferent (outgoing) activity. Figure 7 shows the patterns from a series of t-tests between the  
 290 timings using every possible combination of the two groups for each node. Zero entries mean that  
 291 the t-test was not significant, non-zero entries show the average differences between the mean times  
 292 for each group.

293 We note that FMR1 carriers exhibit much higher inter-peak timings in the thoracic area and the  
 294 lower leg area than the PPD subjects. Both young and elderly controls seem to have much higher  
 295 inter-peak timings in the left arm and hand than PPD patients. Interestingly, FMR1 carriers seem to  
 296 depart further away in their timing profiles from elderly controls than elderly do from the young  
 297 controls. This suggests that the healthy aging process may not significantly alter the afferent or  
 298 efferent rate of activity in any specific area of the body, despite increasing the inter-peak interval  
 299 timing (on average) for the entire body. As we saw earlier (Figure 1) these consistent patterns perhaps  
 300 hint that aging may be spatially non-specific with regards to the rate of activity. On the other hand,  
 301 aging seems to decrease the efferent and afferent activity as well as increase the internal motor  
 302 timings of the system.



303

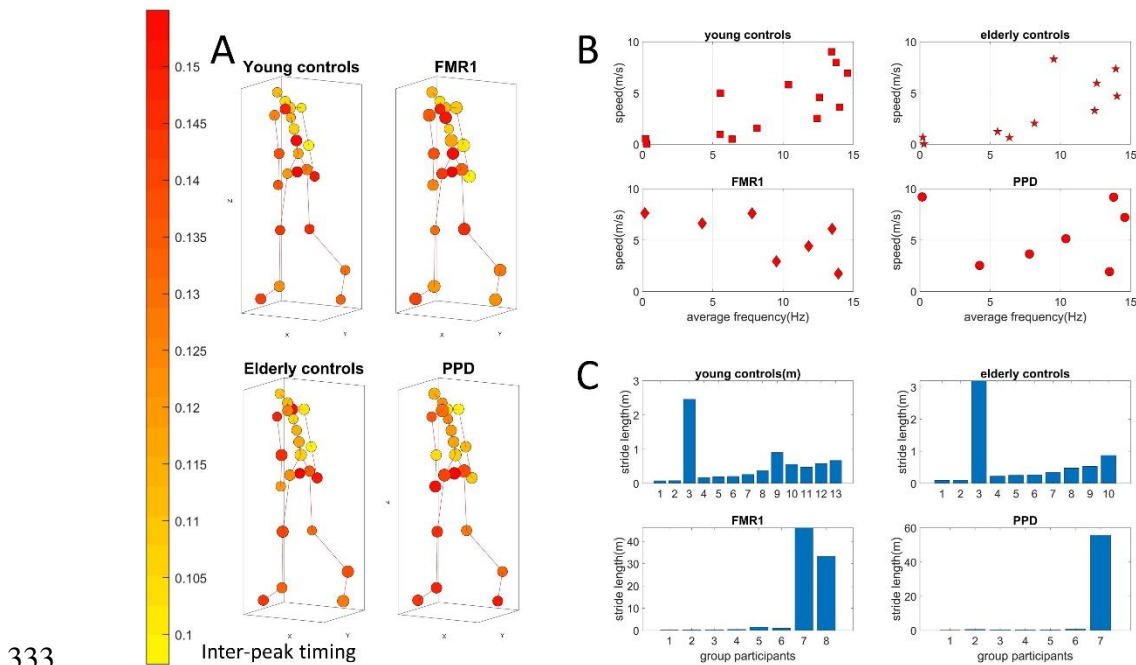
304 **Figure 7: The average differences in inter-peak timings (seconds) taken for each group across all**  
 305 **nodes, reveal separation between groups. A difference of zero (cyan color) indicates no significant**  
 306 **difference ( $p=0.05$ ).**

307 Analyses across the 23 nodes are visualized as an anthropomorphic interconnected network  
 308 representation in Figure 8A. The figure shows the average inter-peak interval times as the color of  
 309 the node. The average cross-coherence output of each node's MMS series is proportional to the size  
 310 of the node. We appreciate differences between the size of the nodes for the different groups, hence  
 311 reflecting differences in the maximum coupling frequencies. Methods Figure 13 shows the analytical  
 312 pipeline to obtain pairwise cross-coherence, along maximal values of the coupling and corresponding  
 313 phase lags and frequencies employed in the derivation of relevant parameter spaces.

314 For each subject, we calculated the average speed of the COM of the lower body, as well as the  
 315 average frequency of the speed time series. We did so, to study how the kinematics of a subject relate  
 316 to the stochastic signatures of the MMS activity. For all groups, except the FMR1 group the speed  
 317 generally increases with respect to the frequency while for the FMR1 carriers the speed decreases.  
 318 This is depicted in Figure 8B.

319 The speed is in m/s and frequency is in Hz, or 1/s. Therefore, speed over frequency has unit of  
 320 meters. Behind this unit analysis, an important biomechanical concept is "hidden". Due to the  
 321 periodic nature of gait, frequency expresses the number of walking cycles or strides per unit time.  
 322 Speed on the other hand, is the average distance traveled by the center of mass of the lower body per  
 323 unit time. Distance over time divided by number of walking cycles over time gives us the distance  
 324 traveled *per stride*. Revisiting Figure 5, we observe that the third dimension, which is speed over  
 325 frequency does not really differ between participants of each group. This indicates that cumulative  
 326 distance per stride could be an invariant quantity by which we could characterize each group. Figure  
 327 8C shows the different patterns of cumulative distance per stride across participants. We note here

328 that the larger the amount of high frequency jitter in the MMS, the larger the accumulation counting  
 329 towards the stride length. As such, some participants in the PPD and FMR1 carriers (both of which  
 330 develop tremor eventually) already show signs of this dysregulation of involuntary jitter in the  
 331 walking patterns.  
 332

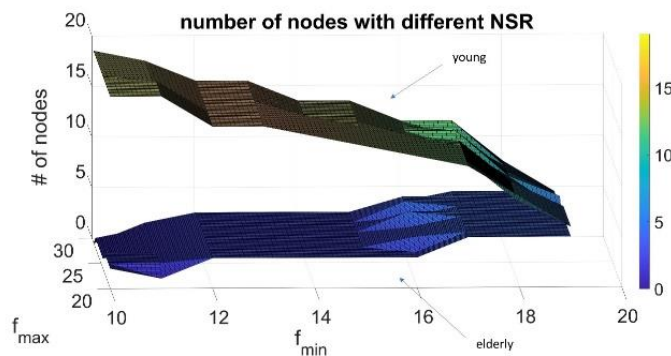


334 **Figure 8: Stride-length differences from speed to frequency ratio obtained from the center of mass**  
 335 **trajectories, separate healthy aging from nervous systems disorders.** (A) Network representation in  
 336 anthropomorphic avatar form. The size of the nodes is proportional to the maximum coupling  
 337 frequency (the one that maximizes cross-coherence) of a node with the rest of the body and the color  
 338 of the nodes is the average time distance (s) between two MMS peaks. (B) Parameter space comparing  
 339 speed vs. frequency. Focusing on the trajectory of the center of mass of the lower body, mean speed  
 340 over mean frequency of the speed time series has a positive upward trend for healthy controls. This  
 341 contrasts to a negative trend in FMR1-carriers and variable trends in PPD. (C) Both types of trends  
 342 and variations span a range of values across both dimensions with stride length periodically  
 343 accumulated differing across groups.

#### 344 *A form of Noise Cancellation with Possible Therapeutic Value*

345 The value of examining feedback loops, timing, and stochastic signatures across the population,  
 346 can be better appreciated within the context of noise cancellation. Noise cancellation helps engineer  
 347 solutions and build accommodations for PPD and other disorders of the nervous systems with  
 348 tremor-related signals. Along those lines, here we investigated how removing different frequency  
 349 bands from the angular speeds of the PPD affected the network dynamics. We tried different  
 350 combinations of low and high limits for the frequency stop band to filter out tremor components (as  
 351 reported by the literature [47](#) and performed *t-tests* between the resulting group and the elderly or  
 352 young control groups for each body node. Then, we measured the number of nodes in which the two  
 353 groups differed significantly in the NSR. We then interpolated a surface on the parameter  
 354 identification data.

355 We report that the optimal tremor removal when comparing to the healthy young controls group  
 356 is for frequencies above 19 Hz, while the optimal tremor removal when comparing to the old controls  
 357 groups is for frequency band with low limits near 10 Hz. Figure 9 shows these differences.

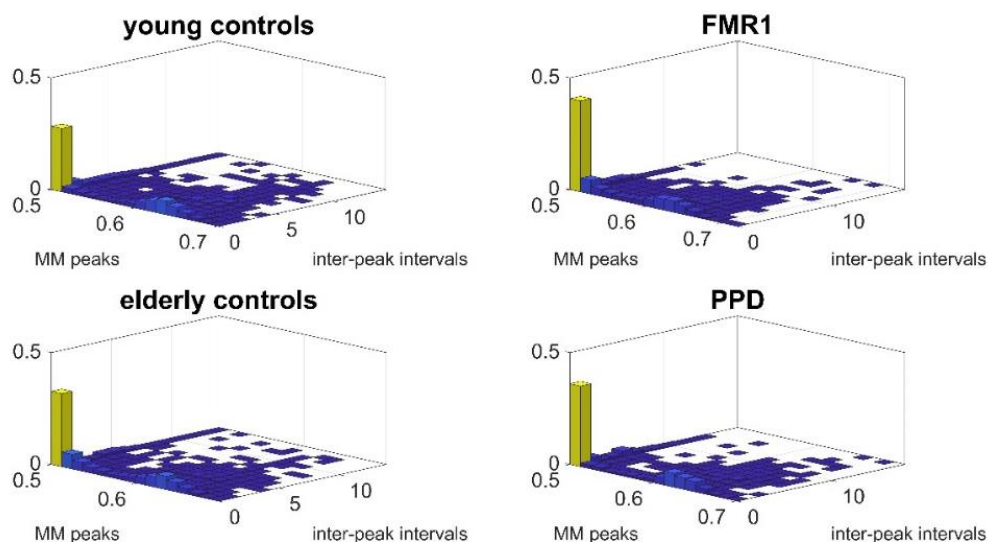


358

359 Figure 9: Noise cancellation by systematic frequency removal in young *vs.* elderly participants. The  
 360 two surface plots show how after removing a component of tremor from the PPD by using band stop  
 361 filtering of the angular velocity for different choices of frequency, the resulting body node  
 362 networks is comparable to the NSR dimension of the young and elderly controls groups. The color bar  
 363 reflects the number of nodes with different NSR that results from the noise cancellation.

### 364 *MMS Amplitude and Timings are Not Independent*

365 Lastly, to further understand the spatio-temporal characteristics of the MMS signal derived from  
 366 the angular speed, we calculated the empirical joint distributions of the MMS inter-peak-interval  
 367 times and the distributions of the MMS amplitude (peak values). We asked if they were independent.  
 368 The results are shown in Figure 10. The complex patterns that emerge indicate that assuming  
 369 independence between the rate of MMS activity and the MMS values is only a first approximation to  
 370 a more complex mechanism that needs to be further investigated.



371

372 Figure 10: Joint empirical distribution of MMS peak values and inter-peak-interval times.

### 373 **Discussion**

374 This study explored walking activity in the context of natural aging and well-established neurological  
 375 conditions found in PPD and FMR1 premutation carriers. We aimed at examining the patterns of  
 376 variability from kinematic parameters that would automatically stratify this random draw of the  
 377 population. Furthermore, we explored the movement trajectories of 23 joints across the body, with  
 378 the purpose of deriving information related to internal temporal lags in information flow. To that

379 end, we framed our problem within the context of causal prediction models of outgoing efferent and  
380 incoming reafference information flow, derived from time series of micro-movement spikes. We  
381 distinguish these internal time lags from external movement times modelled a priori in biomechanics  
382 and robotics. Such trajectories' time profiles are often modelled using the equations of motions to  
383 study human movements' trajectories within some optimization framework (e.g., optimal control  
384 models such as minimum jerk [48](#) minimum torque rate [49](#), minimum energy [50](#), among others.)  
385 Temporal dynamics have been modelled as well in studies of motor control, within the frameworks  
386 of stochastic optimal control and reinforcement learning [51,52](#). In human and animal psychophysics  
387 studies associated with reaction times, temporal information is often derived from computer mouse-  
388 clicks or lever presses, respectively, within the context of perceptual learning, decision making and  
389 other tasks in the cognitive domain [53-56](#). We also distinguish the notion of internal temporal lags  
390 reported here from such studies.

391  
392 To better appreciate the difference between the internal time lags examined here and those from  
393 biomechanics, or from reaction time tasks, we invite the reader to distinguish between a person-  
394 centered perspective, *i.e.*, obtained in personalized and objective manner, and an observer-centered  
395 perspective. The latter makes a statement about the observer's appreciation of actions' trajectory  
396 timing under some a priori defined population statistics, or grand averaging parametric model. It  
397 also imposes a theoretical classical mechanical time-dependent model that is incongruent with  
398 empirical data. Empirical studies show that the geometry and the forces characterizing motion  
399 trajectories are separable, *i.e.* unlike in inanimate rigid bodies in motion, in biological bodies with  
400 nervous systems, the trajectory's temporal dynamics depend on the level of intent that cortical  
401 neurons plan and update online (e.g. [57](#) vs. [38,58-61](#)). The temporal dynamics of motion trajectories also  
402 depend on subcortical regions thought to specify the rate of change in bodily configurations, as the  
403 body transitions from one configuration to the next [62,63](#), and we can model it and study it in PDP [59,61](#).  
404 In contrast to these centrally defined timings, internal time lags examined here, aim at characterizing  
405 temporal dynamics from the efferent and reafferent flow of information across the person's body, at  
406 the periphery. This characterization is done empirically, by estimating the person's stochastic  
407 signatures from the individual fluctuations in the signals' peak amplitudes and inter-peak-intervals'  
408 timings within the framework of causal prediction in time series forecasting analyses [32,64](#) and  
409 augmenting von Holst's principle of reafference to include non-voluntary aspects of actions'  
410 consequences into the feedback that the brain receives from internally self-generated actions.

411  
412 We here define motor timing as the internal timing for which there is a maximal causal relationship  
413 between two neuromotor processes. The internal timing is a stochastic quantity defined as the  
414 random distance in time between two micro-movement-spike peaks. This is different from the  
415 biomechanical physical time of a motor event, measured by an observer-centered external clock  
416 device describing the motion trajectories and / or the decision times of cognitive tasks. As mentioned,  
417 in the former we find families of models that derive temporal dynamics using classical equations of  
418 motion (originally derived for inanimate, rigid bodies). In the latter we find reaction times associated  
419 with decisions and cognitive performance from animate, autonomous agents.

420  
421 While models of biomechanical times cannot account for empirical results in motor control pointing  
422 at a fundamental separation between intended and unintended actions, animal and human models  
423 of reaction times highlight the subjective nature of time perception during reaction tasks in mammals  
424 [65](#) aiming for a general population statement, rather than for an individualized characterization of the  
425 temporal dynamics phenomena. In the present study, we aimed for a person-centered approach that  
426 also led to self-emerging stratification of the cohort. Instead of a priori assuming a given distribution  
427 to characterize the moment-by-moment fluctuations in the walking parameters, we let the data drive  
428 our exploration, revealing maximally informative parameter spaces that automatically separated our  
429 cohort into clusters.

430

431 Indeed, proper parameter spaces allowed us the separate natural aging, PPD and FMR1 premutation  
432 carrier syndrome from the baseline of motor activity in young controls. Of particular interest was the  
433 finding that in natural aging, the lower extremities are compromised, leading to a reduction in the  
434 causal prediction of lower body by upper body extremities. This is accompanied by a lengthening of  
435 the optimal time lags describing information flow derived from fluctuations in movements. Indeed,  
436 the naturally aging person tends to have less communication flow and higher noise-to-signal ratio  
437 than the younger controls. This result was clearly expressed in lower feedback from the legs and feet  
438 to the upper body. The peripheral flow of information appeared to be severely compromised in the  
439 elderly PPD and surprisingly so in much younger FMR1 carriers.

440  
441 The moment-by-moment fluctuations in the peak amplitudes of the MMS offered new ways to  
442 stratify this random draw of the population and clearly distinguish each subgroup in relation to  
443 young controls. Of particular interest here is the multimodal nature of the peaks' distributions  
444 revealing a prevalence of the exponential family that increased with natural aging and was much  
445 more prominent in FMR1 carriers and PPD participants. This result highlights the random,  
446 memoryless nature of the fluctuations in these groups. It also explains the marked reduction in causal  
447 prediction of upper-to-lower body and the lack of feedback from lower to upper body found in the  
448 FMR1 carriers and in the PPD participants. Importantly, the person-centered approach used in this  
449 work was amenable to reveal within each group (young, elderly, PPD and FMR1 carrier) different  
450 subtypes according to the center of position derived from the lower body kinematics. We used these  
451 results to further derive parameter spaces that combined asymmetry in Granger Causality, noise-to-  
452 signal ratio, and distribution skewness to express and to differentiate each group in relation to young  
453 controls. Pair-wise differentiation and patterns were also revealed by the inter-peak timing analyses  
454 of the trunk, arms, and legs regions, with different trends in natural aging *vs.* aging with a nervous  
455 system pathology.

456  
457 The results from this study are amenable to build diagnostic tools using parameter spaces derived  
458 from a simple walking task. Furthermore, the work offers a unifying framework to help predict the  
459 early appearance of large departure from normative ranges in young controls, both for normal aging  
460 and for young participants who are FMR1 carriers. This is important, given the high penetrance of  
461 FX-related syndrome in other neurological conditions across the lifespan. Among these are ASD,  
462 FXTAS and PD. The methods described here offer a new way to detect these gait problems 15-20  
463 years ahead of their clinical onset and as such, could help advance neuroprotective intervention  
464 models.

465  
466 While our analysis uncovered the relationship and similarity between PPD and FMR1 carrier  
467 syndrome, it also sheds light to the process of natural aging and how individuals with PPD age  
468 differently from neurotypicals. Our results indicate that in elderly controls, there is higher overall  
469 causal connectivity in the lower body compared to young controls. It is possible that this is related to  
470 the degeneration of motor functions in the lower body which comes naturally with aging. To preserve  
471 balance and avoid falls, the nervous system will incur in higher cognitive load. As such, natural  
472 walking, a process that is rather automatic in young people becomes cognitively effortful and  
473 requires higher concentration as we age. This higher cognitive (central) demand may be reflected in  
474 the lower body connectivity at the periphery, and poorer lower-to-upper feedback patterns found in  
475 the elderly participants.

476  
477 The results also reveal fundamental differences between PPD and much younger FMR1 carriers, who  
478 nevertheless, also showed a marked reduction in feedback from the lower to the upper extremities.  
479 These two subgroups were far apart in age, yet both revealed large departure from young controls  
480 and timing patterns closer to those of the elderly controls.

481

482 PPDs, show not only a significant increase in lower-body connectivity, but also a marked reduction  
483 in upper-body connectivity. This pattern suggests that the degeneration of motor control in PPD is  
484 not limited to the lower body, but that in fact, it is a disease that affects the motor system in a general  
485 and systemic way. A higher cognitive load is required to control the lower body which as a side effect  
486 may result in poor connectivity in the upper body, and poor systemic coordination with impaired  
487 kinesthetic sensory feedback. Interestingly, when comparing how the inter-peak timings of each body  
488 node differ between groups, we can conclude that in that sense, the elderly controls and the FMR1  
489 carriers are almost identical to young controls. On the other hand, PPDs have significant different  
490 inter-peak intervals' timings than young controls. This not only shows the departure of PPD from  
491 natural aging, but also shows that despite the Parkinsonian symptoms of FMR1 syndrome, the latter  
492 is still a fundamentally different condition than PPD.

493

494 Finally, as a potential actionable application of the present work to mitigate the high levels of noise  
495 found in the walking patterns of PPD and FMR1 carriers, we used the relationship that Granger's  
496 causal prediction methods offer between frequency and time domains. Inspired by Granger's  
497 approach, we developed a network-connectivity based model of noise cancellation. Specifically, we  
498 systematically removed frequencies reportedly associated with tremor in the literature [47](#) and  
499 quantified the outcomes of this systematic removal on the noise portrait derived from the time series  
500 analyses of angular speed peaks of walking patterns. We found differing ranges of optimal tremor  
501 removal relative to healthy young *vs.* elderly controls group. The former reveal optimal ranges for  
502 frequencies above 19 Hz, while the latter showed frequency band with lower limits, near 10 Hz. More  
503 exploration of these aspects of noise cancellation are warranted, yet using the present approach  
504 exploring internal optimal time lags within the context of causal prediction, we open new avenues of  
505 personalized support tailored to PPD and FMR1 carriers of different age groups.

506

507 Besides the frequency-time relations highlighted in the above exploration, the work also revealed  
508 important spatio-temporal features of the MMS. Namely, through examination of the joint empirical  
509 distributions of MMS derived from fluctuations in the angular speed peaks' amplitude and the MMS  
510 derived from the fluctuations in inter-peaks-interval timings, we found interdependences and  
511 complex patterns rendering invalid the common assumption of independence in the spikes data. This  
512 result also opens new questions about common assumptions of stationarity and homogeneity in the  
513 data. Future empirical and theoretical work will be necessary to advance this important area of  
514 research vital for interpretation and statistical inference of behavioral phenomena.

515

516 In summary, we offer a new unifying framework to stratify a random draw of the population based  
517 on natural walking patterns, identify subtypes within each group and anticipate pathologies of the  
518 nervous systems bound to appear with natural aging and with genetic-based differences.  
519 Furthermore, we provide actionable models of noise cancellation to build supportive interventions  
520 with the potential to enhance causal prediction and feedback from movements and to improve  
521 internal temporal lags of information flow. This could help lower the cognitive load that an otherwise  
522 automatic walking task may cause as we naturally age, as we acquire Parkinsonism, or in cases where  
523 the person inherits a genetic mutation. Our personalized approach and our new definition of internal  
524 motor-sensing timings can provide true targeted interventions to help mitigate and protect against  
525 neurodegeneration.

526

## 527 **Materials and Methods**

528 This study was approved by the Rutgers Institutional Review Board (IRB) abiding by the precepts of  
529 the Helsinki Act. Thirty-seven patients were included out of thirty-eight participants (age mean 37.24,  
530 std 21.39, 10 males and 28 females). There was sensor malfunctioning for one elderly participant, so  
531 we did not include him in the analysis. Patients were recruited through the clinical\_trials.gov site,  
532 the Robert Wood Johnson clinic, and the New Jersey Autism Center of Excellence

533 (https://www.njace.us/). Informed consent was obtained from the participants according to our  
 534 Rutgers University IRB-approved protocol. Different aspects of these data unrelated to gait, were  
 535 previously published [8,9,66](#).

### 536 2.1. Experimental Design and Statistical Analyses

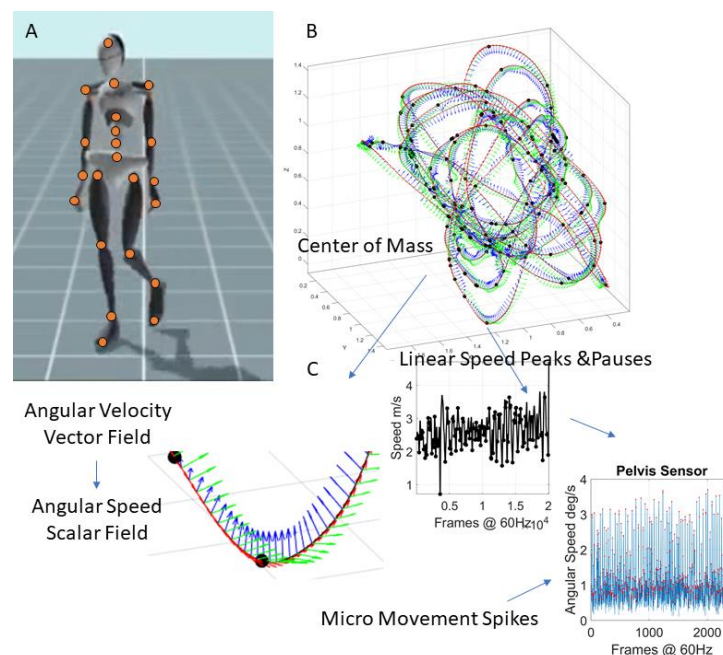
537 Participants wore the XSens system (17 wearable sensors across the body collecting position,  
 538 orientation, and acceleration at 60Hz, from 23 joints depicted in Figure 11A). In-house MATLAB  
 539 routines were used to implement the Frenet-Serret frame [67](#) and derive various kinematics  
 540 parameters. Position was used to derive linear velocity fields, which were converted to scalar fields  
 541 of speed (m/s). Then maxima and minima were obtained as landmarks to track the speed of the center  
 542 of mass (e.g., Figure 11B) (obtained by replacing mass with length in the original equation 1).

543

$$544 V_{com} = \frac{\sum_{i=1}^{23} V_i L_i}{\sum_{i=1}^{23} L_i} \quad (1)$$

545

546 Time series of the latter were scaled, and the micro-movement spikes (MMS) obtained in further  
 547 analyses (Figure 11C).



548

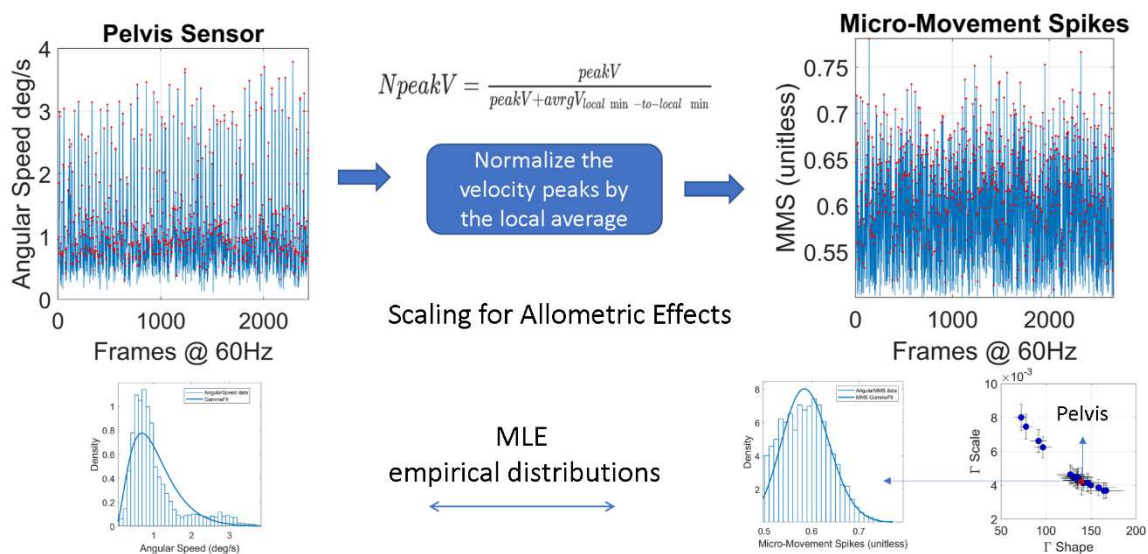
549 **Figure 11: Methods Figure.** (A) Data acquisition using a grid of wearable sensors calibrating position  
 550 and orientation in real time and sampling changes of position in time, at 60Hz. (B) Center of Mass  
 551 trajectories (m) in 3D parameterized using the Frenet-Serret frame to study geometric aspects of the  
 552 curve. (C) Linear speed used to mark pauses and peaks along the curve, thus allowing us to express  
 553 behavioral landmarks along other kinematics parameters such as the angular speed quantifying  
 554 bodily rates of 23 joints' rotations. The MMS are derived from the fluctuations in angular speed  
 555 amplitude. Red dots mark peaks (transitions of speed slope from positive to negative.)

556 **Micromovement Spikes (MMS):** The MMS are defined as the normalized peaks of any  
 557 kinematics time series of the fluctuations in amplitude, as the signal deviates from the mean  
 558 amplitude. Specifically, to obtain the micromovements time series from the angular speed time series

559 we first calculate the peaks. Each peak is then normalized by the local average speed of the speed, *i.e.*  
 560 the average value of the two minima before and after the peak (equation 2).

561 
$$N_{peak} = \frac{peakV}{peakV + avgV_{local\ min\ -to-\ local\ min}} \quad (2)$$

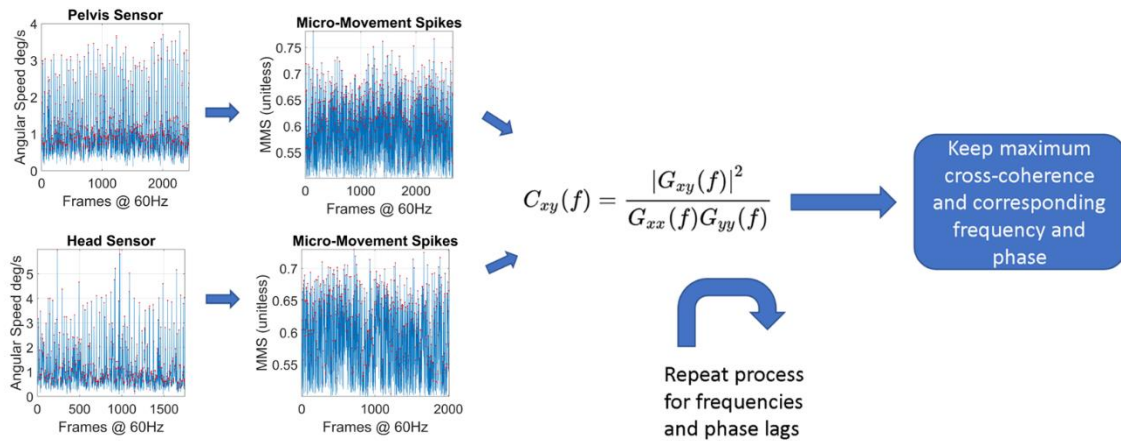
562 It has been shown that the resulting MMS time series follows the generalized gamma  
 563 distribution in human motion and applied to gait <sup>33,68</sup>. Then, from the resulting time series we subtract  
 564 the gamma fitted mean (fitted using maximum likelihood estimation, MLE). The MMS time series  
 565 allows us to extract information independent of the body dimensions of the subject. When tracking  
 566 them continuously, we can use them as a peripheral proxy of the efferent and afferent activity of the  
 567 central nervous system. Figure 12 shows the pipeline describing the MMS extraction from the sensor  
 568 data.



569  
 570 **Figure 12:** The MMS time series extraction from the angular speed tracking stochastic trajectories from  
 571 all joints (red dot marks the pelvis for instance.)

572 *Cross-coherence:* The cross-coherence between two times series (assumed to be the realizations of  
 573 unknown stochastic processes) is defined as the cross-spectral density between the two series  
 574 normalized by the product of their auto-spectral densities <sup>69</sup>. Since human motion is non-linear, in  
 575 this study we use cross-coherence to quantify the similarity between any two body nodes' MMS time  
 576 series in the frequency domain. We then identify the frequency for which the cross-coherence  
 577 function is maximized.

578



579

580 **Figure 13:** The pipeline for the calculation of the maximum cross-coherence and the frequency for  
 581 which it is maximized.

582 *Mean frequency:* The mean frequency of a spectrogram  $P(f)$  is calculated as:

$$583 \quad f_{mean} = \frac{\sum_{j=1}^N f_j P_j}{\sum_{j=1}^N P_j} \quad (3)$$

584 Where  $f_j$  is the central frequency of the  $j$ -th bin of the spectrum and  $P_j$  the corresponding value of  
 585 the power spectral density.  $N$  is the total number of bins [20](#).

586 *Granger causality:* The MMS serve as a proxy to reflect the inner activity of the nervous system  
 587 as it is expressed by the kinematics of the various body parts. Hence, we now have a network of times  
 588 series (23 nodes) that provide information about the mechanisms of the CNS to control the peripheral  
 589 activity for each subject and each group of subjects. Specifically, we are interested in the relationship  
 590 between two time series of MMS. Traditional concepts, such as mutual information, cross-correlation  
 591 and cross-coherence are being widely used to estimate the mutual information between two  
 592 stochastic processes [21](#), or to investigate how one relates to the other in the time or frequency domain  
 593 [9,22,23](#). However, they provide no information about the direction in which the information flows, i.e.,  
 594 which stochastic process is the cause and which the effect.

595 Other concepts such as Transfer Entropy (TE) and Granger Causality (GC) give us both the  
 596 direction in which the information flows, as well as the quantity of the information flowing from the  
 597 causal stochastic process to the effector stochastic process [24](#). In fact, in the case of gaussian processes  
 598 these two are equivalent [25](#). TE does not require a model and is based on information theory concepts.  
 599 GC on the other hand, requires fitting an AR model of order  $N$  to the time series data.

600 For the purposes of this paper, we choose the concept of GC. There are two reasons for our  
 601 choice. First, GC has a much smaller computational complexity than TE. Second, assuming an  
 602 autoregressive model can help us estimate the response lags between different body activities. We  
 603 define the response lag as the number of MM peaks needed for information to flow from the afferent  
 604 input of a body part to the efferent output of another body part. To explain how we estimate the  
 605 response lags between the activities of any two body parts we must first explain the concept of GC.

606 Granger, in his original paper defined causality for a pair of stochastic processes  $X$  and  $Y$  in a  
 607 solid, mathematical way [45](#). Assume we have a closed system or “universe” in which all available  
 608 information is contained in the stochastic processes  $X$  and  $Y$  and let  $X_t$  and  $Y_t$  be the realizations of  
 609 these stochastic processes up to time  $t$ . Let  $U_t$  be all the information accumulated from both time

610 series up to  $t-1$ . U-Y implies all information apart from Y. Granger gave the following definition of  
 611 causality. Using his own words [45](#):

612 “If  $\sigma^2(X|U) < \sigma^2(X|U - Y)$ , we say that Y is causing X, denoted by  $Y_t \Rightarrow X_t$ . We say that  $Y_t$  is  
 613 causing  $X_t$ , if we are better able to predict  $X_t$  using all available information than if the information  
 614 apart from  $Y_t$  has been used.”

615  
 616 The operator  $A|B$ , where A, B are stochastic processes means the “construction” of a model  
 617 where A is predicted from B. The operator  $\sigma^2(A|B)$  means the variance of the error of the model  
 618  $A|B$ . Granger’s definition implies that if a model that predicts the dynamic behavior of X that does  
 619 not include Y, has a greater on average error than a model that includes Y, then Y “causes” X in that  
 620 sense. Furthermore, Granger gave a formal definition of “causality lag”, which simply informs us  
 621 how far in the past we should consider samples of X and Y in our prediction to get an optimal  
 622 prediction.

623  
 624 “If  $Y_t \Rightarrow X_t$ , we define the (integer) causality lag m to be the least value of k such that  
 625  $\sigma^2(X|U - Y(k)) < \sigma^2(X|U - Y(k + 1))$ . Thus, knowing the values  $Y_{t-j}, j=0,1,\dots,m-1$ , will be of no help in  
 626 improving the prediction of  $X_t$ .”

627  
 628 Simply put, the concept of causality lag refers to the maximum lag in the past of the realization  
 629 of the stochastic process Y, beyond which, including more past samples will result in a bigger  
 630 prediction error.

631  
 632 Granger also referred to “instantaneous causality”, which simply means that in the prediction  
 633 we also include the present values of the stochastic processes. In our present work, due to the non-  
 634 instantaneous nature of neural information, we assume that prediction should include only the past  
 635 values. In his solution to the problem of estimating causality for econometric time series, Granger  
 636 assumed autoregressive models of some appropriate order and used techniques of spectral analysis  
 637 [64](#). He defined two models, one simple causal model that includes the past samples of both time series  
 638 and one non-causal model that includes only the effector process. For our purposes, we formulated  
 639 our own model and approach to Granger causality which allows us to quantify the internal motor  
 640 timings of the system.

641  
 642 Let X and Y be the two univariate stochastic processes and  $X_n, Y_n$  the corresponding time series  
 643 we obtained from our sensors. For a choice l of the internal time lag of the system, we assume the  
 644 non-causal and causal models:

$$645 \quad x_n = a_1 x_{n-l} + w_{1n} \quad (4)$$

$$646 \quad x_n = a_2 x_{n-l} + b y_{n-l} + w_{2n} \quad (5)$$

647  
 648  
 649  
 650 Where  $w_1, w_2$  are independent discrete time AWGN (additive white gaussian noise) processes  
 651 and  $a_1, a_2, b$  constants we want to estimate from the statistical properties of our data. We also make  
 652 the hypothesis that the noise processes are independent from X and Y. Assuming that the noise  
 653 processes are gaussian implies they have zero means. To apply this model without loss of generality  
 654 we simply pre-process our data by centering them around zero.

655 To proceed, we multiply equation (4) with  $x_n$  and we get:

$$656 \quad x_n^2 = a x_n x_{n-l} + w_{1n} x_n \quad (6)$$

657  
 658  
 659 Applying the expectation operator  $E(\cdot)$  on both sides of equation (6):

$$660 \quad E\{x_n^2\} = aE\{x_n x_{n-l}\} + E\{w_{1n} x_n\} \quad (7)$$

661  
662  
663  
664  
665  
666  
667  
668  
669  
670  
671  
672  
673  
674  
675  
676  
677  
678  
679  
680  
681  
682  
683  
684  
685  
686  
687  
688  
689  
690  
691  
692  
693  
694  
695  
696  
697  
698  
699  
700  
701  
702  
703  
704  
705  
706  
707  
708  
709  
710  
711  
712

Since noise  $w_1$  and the process  $X$  are independent, it means they are uncorrelated. Therefore:

$$E\{x_n^2\} = aE\{x_n x_{n-1}\}$$

From which we get an estimate for the constant  $a$ :

$$a = \frac{E\{x_n^2\}}{E\{x_n x_{n-1}\}} = \frac{R_{xx}(0)}{R_{xx}(l)} \quad (8)$$

Where  $R_{xx}(\tau) = E\{x_n x_{n-\tau}\}$  is the autocorrelation function of  $X$ .

We continue by multiplying (5) with  $x_n$ :

$$x_n^2 = a_2 x_{n-1} x_n + b y_{n-1} x_n + w_{2n} x_n \quad (9)$$

Also, we multiply (5) with  $x_{n-1}$ :

$$x_n x_{n-1} = a_2 x_{n-1}^2 + b y_{n-1} x_{n-1} + w_{2n} x_{n-1} \quad (10)$$

Taking the expectation on both sides of (9) and (10), since  $X$  and  $Y$  are uncorrelated, we finally arrive to the system of equations:

$$R_{xx}(0) = a_2 R_{xx}(l) + b R_{xy}(l)$$

$$R_{xx}(l) = a_2 R_{xx}(0) + b R_{xy}(0) \quad (11)$$

Where  $R_{xy}(\tau) = E\{x_n y_{n-\tau}\}$  is the cross-correlation function between  $X$  and  $Y$ .

Assuming (11) has a solution, we can estimate  $a_2, b$ .

The final step in our analysis is to find the variances of the noises.

We square equations (4) and (5):

$$x_n^2 = a_1^2 x_{n-1}^2 + w_{1n}^2 + 2a_1 x_{n-1} w_{1n} \quad (12)$$

$$x_n^2 = a_2^2 x_{n-1}^2 + b^2 y_{n-1}^2 + w_{2n}^2 + 2a_2 x_{n-1} b y_{n-1} + 2(a_2 x_{n-1} w_{2n} + b y_{n-1} w_{2n}) \quad (13)$$

Applying the expectation in both sides, since the noises are independent of the processes, all cross-correlation terms between processes and noises are zero, therefore:

$$E\{w_{1n}^2\} = E\{x_n^2\} - a_1^2 E\{x_{n-1}^2\} \quad (14)$$

$$E\{w_{2n}^2\} = E\{x_n^2\} - a_2^2 E\{x_{n-1}^2\} - b^2 E\{y_{n-1}^2\} - 2a_2 b E\{x_{n-1} y_{n-1}\} \quad (15)$$

Since the variance of a noise processes  $w$  is  $\sigma^2 = E\{(w - w_{mean})^2\}$ , in our case where the noises are zero mean, eventually:

$$\sigma_1^2 = R_{xx}(0) - a_1^2 R_{xx}(0) = (1 - a_1^2) R_{xx}(0) \quad (16)$$

$$\sigma_2^2 = R_{xx}(0) - a_2^2 R_{xx}(0) - b^2 R_{yy}(0) - 2a_2 b R_{xy}(0) = (1 - a_2^2) R_{xx}(0) - 2a_2 b R_{xy}(0) \quad (17)$$

713 Thus, solving system (9) gives us the constants of the system for a given choice of lag and then  
 714 equations (16), (17) give us the errors of the non-causal and causal models. Following the logarithmic  
 715 definition of causality [76](#):  
 716

717 
$$GC = \log \left( \frac{\sigma_1^2}{\sigma_2^2} \right) \quad (18)$$

718  
 719 If the causal model better predicts the behavior of  $X$  for a given internal motor lag,  $\sigma_2^2 < \sigma_1^2$   
 720 then  $GC > 0$ .

721 A standard causal autoregressive (AR) model of order one is of the form:

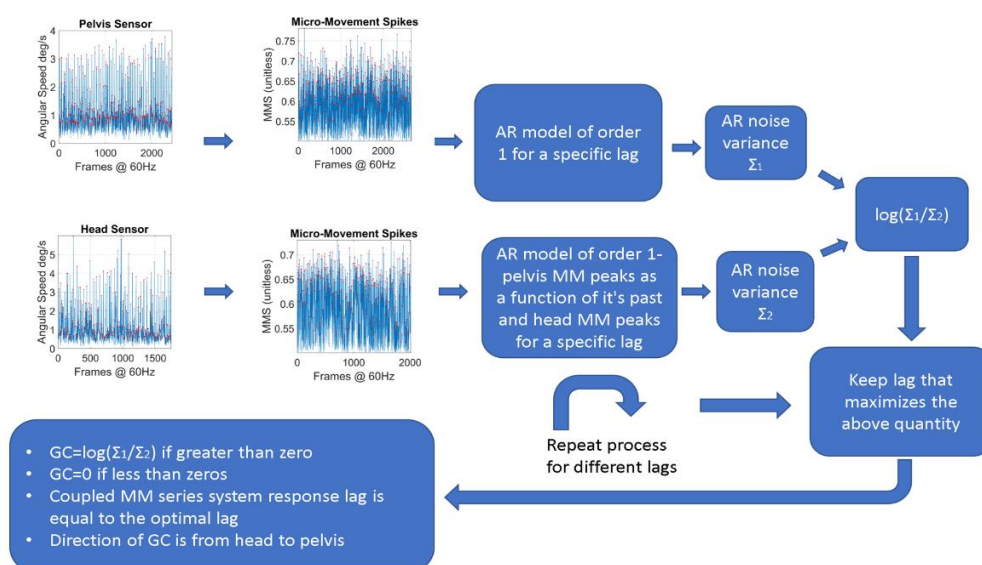
722  
 723 
$$x_n = ax_{n-1} + by_{n-1} + noise$$

724  
 725 Which is order 1. However, what is the physical meaning of “order 1”? It means we assume the  
 726 previous sample, one lag in the past of  $X$ , contribute to the prediction of  $X$ . It is an arbitrary quantity  
 727 when we consider it independently of the sampling rate  $F_s$  of our sensors. In context however, one  
 728 lag is  $\frac{1}{F_s}$  seconds, which is the fundamental unit of time of our system. In our model, we assume:

729  
 730 
$$x_n = ax_{n-l} + by_{n-l} + noise$$

731  
 732 This can still be assumed an autoregressive model of order 1 in which the fundamental unit of  
 733 time is not one sampling period but  $l$  sampling periods. Different choices of  $l$  will give  
 734 autoregressive models for different *time scales*. The time scale  $l$  for which causality is maximized is  
 735 our definition of “internal motor timing”, because at this time scale, we have the maximum flow of  
 736 information from  $Y$  to  $X$ .

737 We make the following hypothesis. At any given moment, the process  $Y_t$  transmits information  
 738 to the process  $X_t$  through the CNS. The response lag between the two processes is the time needed  
 739 for information to travel from the afferent process  $Y_t$  to the efferent process  $X_t$ . Following this train of  
 740 thought we can assume that the lag parameter of the AR models that maximizes the GC is the best  
 741 estimation of the corresponding response time between  $X_t$  and  $Y_t$ . Therefore, we propose the  
 742 following pipeline of analysis to find the maximum GC and estimate the response lags between any  
 743 two sensor MMS time series of the subjects (Figure 14).



744  
 745 **Figure 14:** Pipeline for the estimation of the Granger Causality and Response time values between  
 746 two body parts.

747 **References**

- 748 1 Ambar Akkaoui, M., Geoffroy, P. A., Roze, E., Degos, B. & Garcin, B. Functional Motor Symptoms in  
749 Parkinson's Disease and Functional Parkinsonism: A Systematic Review. *J Neuropsychiatry Clin Neurosci*  
750 **32**, 4-13, doi:10.1176/appi.neuropsych.19030058 (2020).
- 751 2 Chien, J. H., Yentes, J., Stergiou, N. & Siu, K. C. The Effect of Walking Speed on Gait Variability in  
752 Healthy Young, Middle-aged and Elderly Individuals. *J Phys Act Nutr Rehabil* **2015** (2015).
- 753 3 Doridam, J., Mongin, M. & Degos, B. Movement disorders in the elderly. *Geriatr Psychol Neuropsychiatr*  
754 *Vieil* **17**, 395-404, doi:10.1684/pnv.2019.0825 (2019).
- 755 4 Lenardt, M. H. et al. Gait speed and cognitive score in elderly users of the primary care service. *Rev Bras*  
756 *Enferm* **68**, 1163-1168, doi:10.1590/0034-7167.2015680623i (2015).
- 757 5 Parisi, F. et al. Body-Sensor-Network-Based Kinematic Characterization and Comparative Outlook of  
758 UPDRS Scoring in Leg Agility, Sit-to-Stand, and Gait Tasks in Parkinson's Disease. *IEEE J Biomed Health*  
759 *Inform* **19**, 1777-1793, doi:10.1109/JBHI.2015.2472640 (2015).
- 760 6 Park, S. H. et al. Functional motor control deficits in older FMR1 premutation carriers. *Exp Brain Res*  
761 **237**, 2269-2278, doi:10.1007/s00221-019-05566-3 (2019).
- 762 7 Wang, Z., Khemani, P., Schmitt, L. M., Lui, S. & Mosconi, M. W. Static and dynamic postural control  
763 deficits in aging fragile X mental retardation 1 (FMR1) gene premutation carriers. *J Neurodev Disord* **11**,  
764 **2**, doi:10.1186/s11689-018-9261-x (2019).
- 765 8 Ryu, J., Vero, J., Dobkin, R. D. & Torres, E. B. Dynamic Digital Biomarkers of Motor and Cognitive  
766 Function in Parkinson's Disease. *J Vis Exp*, doi:10.3791/59827 (2019).
- 767 9 Ryu, J., Vero, J. & Torres, E. B. in *MOCO '17: Proceedings of the 4th International Conference on Movement*  
768 *Computing.* 1-8 (ACM).
- 769 10 Torres, E. B. et al. Characterization of the Statistical Signatures of Micro-Movements Underlying  
770 Natural Gait Patterns in Children with Phelan McDermid Syndrome: Towards Precision-Phenotyping  
771 of Behavior in ASD. *Front Integr Neurosci* **10**, **22**, doi:10.3389/fnint.2016.00022 (2016).
- 772 11 Torres, E. B. Reframing Psychiatry for Precision Medicine. *J Pers Med* **10**, doi:10.3390/jpm10040144  
773 (2020).
- 774 12 Fujita-Jimbo, E. et al. Mutation in Parkinson disease-associated, G-protein-coupled receptor 37  
775 (GPR37/PaelR) is related to autism spectrum disorder. *PLoS One* **7**, e51155,  
776 doi:10.1371/journal.pone.0051155 (2012).
- 777 13 Glessner, J. T. et al. Autism genome-wide copy number variation reveals ubiquitin and neuronal genes.  
778 *Nature* **459**, 569-573, doi:10.1038/nature07953 (2009).
- 779 14 Xie, F. et al. Advances in the Research of Risk Factors and Prodromal Biomarkers of Parkinson's Disease.  
780 *ACS Chem Neurosci* **10**, 973-990, doi:10.1021/acschemneuro.8b00520 (2019).
- 781 15 Amadori, K. & Steiner, T. [Parkinson's syndromes in geriatric patients : Epidemiological, clinical and  
782 therapeutic characteristics]. *Nervenarzt* **90**, 1279-1291, doi:10.1007/s00115-019-00825-8 (2019).
- 783 16 Lord, C. et al. Autism diagnostic observation schedule: a standardized observation of communicative  
784 and social behavior. *J Autism Dev Disord* **19**, 185-212 (1989).
- 785 17 (American Psychiatric Association, Arlington, VA, 2013).
- 786 18 Hagerman, R., Hoem, G. & Hagerman, P. Fragile X and autism: Intertwined at the molecular level  
787 leading to targeted treatments. *Mol Autism* **1**, **12**, doi:10.1186/2040-2392-1-12 (2010).
- 788 19 Hall, D. A. et al. Clinimetric Properties of the Fragile X-associated Tremor Ataxia Syndrome Rating  
789 Scale. *Mov Disord Clin Pract* **6**, 120-124, doi:10.1002/mdc3.12708 (2019).

- 790 20 Leehey, M. A. *et al.* FMR1 CGG repeat length predicts motor dysfunction in premutation carriers.  
791 *Neurology* **70**, 1397-1402, doi:10.1212/01.wnl.0000281692.98200.f5 (2008).
- 792 21 Torres, E. B., Caballero, C. & Mistry, S. Aging with Autism Departs Greatly from Typical Aging. *Sensors*  
793 (*Basel*) **20**, doi:10.3390/s20020572 (2020).
- 794 22 Torres, E. B. & Denisova, K. Motor noise is rich signal in autism research and pharmacological  
795 treatments. *Sci Rep* **6**, 37422, doi:10.1038/srep37422 (2016).
- 796 23 de Rijk, M. C. *et al.* Prevalence of parkinsonism and Parkinson's disease in Europe: the  
797 EUROPARKINSON Collaborative Study. European Community Concerted Action on the  
798 Epidemiology of Parkinson's disease. *J Neurol Neurosurg Psychiatry* **62**, 10-15, doi:10.1136/jnnp.62.1.10  
799 (1997).
- 800 24 Starkstein, S., Gellar, S., Parlier, M., Payne, L. & Piven, J. High rates of parkinsonism in adults with  
801 autism. *J Neurodev Disord* **7**, 29, doi:10.1186/s11689-015-9125-6 (2015).
- 802 25 Caballero, C., Mistry, S. & Torres, E. B. Age-Dependent Statistical Changes of Involuntary Head Motion  
803 Signatures Across Autism and Controls of the ABIDE Repository. *Front. Integr. Neurosci.* **14**, 1-14,  
804 doi:doi: 10.3389/fnint.2020.00023 (2020).
- 805 26 Hall, D. A., Howard, K., Hagerman, R. & Leehey, M. A. Parkinsonism in FMR1 premutation carriers  
806 may be indistinguishable from Parkinson disease. *Parkinsonism Relat Disord* **15**, 156-159,  
807 doi:10.1016/j.parkreldis.2008.04.037 (2009).
- 808 27 Wang, L. W., Berry-Kravis, E. & Hagerman, R. J. Fragile X: leading the way for targeted treatments in  
809 autism. *Neurotherapeutics* **7**, 264-274, doi:10.1016/j.nurt.2010.05.005 (2010).
- 810 28 Godoi, B. B. *et al.* Parkinson's disease and wearable devices, new perspectives for a public health issue:  
811 an integrative literature review. *Rev Assoc Med Bras (1992)* **65**, 1413-1420, doi:10.1590/1806-  
812 9282.65.11.1413 (2019).
- 813 29 O'Keefe, C. *et al.* Complexity based measures of postural stability provide novel evidence of functional  
814 decline in fragile X premutation carriers. *J Neuroeng Rehabil* **16**, 87, doi:10.1186/s12984-019-0560-6 (2019).
- 815 30 Schmitt, A. C., Daniels, J. N., Baudendistel, S. T., Okun, M. S. & Hass, C. J. The Primary Gait Screen in  
816 Parkinson's disease: Comparison to standardized measures. *Gait Posture* **73**, 71-73,  
817 doi:10.1016/j.gaitpost.2019.07.132 (2019).
- 818 31 Torres, E. B. *et al.* Toward Precision Psychiatry: Statistical Platform for the Personalized  
819 Characterization of Natural Behaviors. *Front Neurol* **7**, 8, doi:10.3389/fneur.2016.00008 (2016).
- 820 32 Granger, C. W. J. *Spectral analysis of economic time series.* (Princeton University Press, 1964).
- 821 33 Torres, E. B. *et al.* Autism: the micro-movement perspective. *Front Integr Neurosci* **7**, 32,  
822 doi:10.3389/fnint.2013.00032 (2013).
- 823 34 Von Holst E. & H., M. in *Perceptual Processing: Stimulus equivalence and pattern recognition* (ed ed Dodwell  
824 PC) 41-72 (Appleton-Century-Crofts, 1950).
- 825 35 Torres, E. B. Two classes of movements in motor control. *Exp Brain Res* **215**, 269-283, doi:10.1007/s00221-  
826 011-2892-8 (2011).
- 827 36 Wolpert, D. M., Miall, R. C. & Kawato, M. Internal models in the cerebellum. *Trends Cogn Sci* **2**, 338-347,  
828 doi:10.1016/s1364-6613(98)01221-2 (1998).
- 829 37 Kawato, M. & Wolpert, D. Internal models for motor control. *Novartis Found Symp* **218**, 291-304;  
830 discussion 304-297, doi:10.1002/9780470515563.ch16 (1998).
- 831 38 Ryu, J. & Torres, E. The Autonomic Nervous System Differentiates between Levels of Motor Intent and  
832 End Effector. *J Pers Med* **10**, doi:10.3390/jpm10030076 (2020).

- 833 39 Torres, E. B. System and method for determining amount of volition in a subject. US patent (2017, Oct.  
834 19).
- 835 40 Torres, E. B. Signatures of movement variability anticipate hand speed according to levels of intent.  
836 *Behav Brain Funct* **9**, 10, doi:10.1186/1744-9081-9-10 (2013).
- 837 41 Anderson, S. R. *et al.* Adaptive cancelation of self-generated sensory signals in a whisking robot. *IEEE*  
838 *Transactions on Robotics* **26**, 1065-1076 (2010).
- 839 42 Anderson, S. R. *et al.* An internal model architecture for novelty detection: implications for cerebellar  
840 and collicular roles in sensory processing. *PLoS One* **7**, e44560 (2012).
- 841 43 Bays, P. M. & Wolpert, D. M. Computational principles of sensorimotor control that minimize  
842 uncertainty and variability. *The Journal of physiology* **578**, 387-396 (2007).
- 843 44 Habra, T., Grotz, M., Sippel, D., Asfour, T. & Ronsse, R. in *2017 IEEE-RAS 17th International Conference*  
844 *on Humanoid Robotics (Humanoids)*. 47-54 (IEEE).
- 845 45 Granger, C. W. J. Investigating Causal Relations by Econometric Models and Cross-spectral Methods.  
846 *Econometrica* **37**, 424-438 (1969).
- 847 46 Hartigan, J. A. & Hartigan, P. M. The Dip Test of Unimodality. *The Annals of Statistics* **13**, 70-84 (1985).
- 848 47 Lee, H. J. *et al.* Tremor frequency characteristics in Parkinson's disease under resting-state and stress-  
849 state conditions. *Journal of the neurological sciences* **362**, 272-277 (2016).
- 850 48 Viviani, P. & Flash, T. Minimum-jerk, two-thirds power law, and isochrony: converging approaches to  
851 movement planning. *Journal of Experimental Psychology: Human Perception and Performance* **21**, 32 (1995).
- 852 49 Kawato, M., Maeda, Y., Uno, Y. & Suzuki, R. Trajectory formation of arm movement by cascade neural  
853 network model based on minimum torque-change criterion. *Biological cybernetics* **62**, 275-288 (1990).
- 854 50 Alexander, R. M. A minimum energy cost hypothesis for human arm trajectories. *Biological cybernetics*  
855 **76**, 97-105 (1997).
- 856 51 Doya, K. Complementary roles of basal ganglia and cerebellum in learning and motor control. *Current*  
857 *opinion in neurobiology* **10**, 732-739 (2000).
- 858 52 Peters, J. & Schaal, S. Reinforcement learning of motor skills with policy gradients. *Neural networks* **21**,  
859 682-697 (2008).
- 860 53 Buhusi, C. V. & Meck, W. H. What makes us tick? Functional and neural mechanisms of interval timing.  
861 *Nature reviews neuroscience* **6**, 755-765 (2005).
- 862 54 Lestienne, R. Spike timing, synchronization and information processing on the sensory side of the  
863 central nervous system. *Progress in neurobiology* **65**, 545-591 (2001).
- 864 55 Machado, A., Malheiro, M. T. & Erlhagen, W. Learning to time: A perspective. *Journal of the experimental*  
865 *analysis of behavior* **92**, 423-458 (2009).
- 866 56 Simen, P., Rivest, F., Ludvig, E. A., Balci, F. & Killeen, P. Timescale invariance in the pacemaker-  
867 accumulator family of timing models. *Timing & Time Perception* **1**, 159-188 (2013).
- 868 57 Flash, T., Hogan, N. The coordination of arm movements: an experimentally confirmed mathematical  
869 model. *The Journal of Neuroscience* **5**, 1688-1703 (1985).
- 870 58 Torres, E. B., Quiñero, R., Cui, H. & Buneo, C. A. Neural correlates of learning and trajectory  
871 planning in the posterior parietal cortex. *Front Integr Neurosci* **7**, 39, doi:10.3389/fnint.2013.00039 (2013).
- 872 59 Torres, E. B., Zipser, D. Reaching to Grasp with a Multi-jointed Arm (I): A Computational Model.  
873 *Journal of Neurophysiology* **88**, 1-13 (2002).
- 874 60 Torres, E. & Andersen, R. Space-time separation during obstacle-avoidance learning in monkeys. *J*  
875 *Neurophysiol* **96**, 2613-2632, doi:10.1152/jn.00188.2006 (2006).

- 876 61 Torres, E. B., Heilman, K. M. & Poizner, H. Impaired endogenously evoked automated reaching in  
877 Parkinson's disease. *J Neurosci* **31**, 17848-17863, doi:10.1523/JNEUROSCI.1150-11.2011 (2011).
- 878 62 Yin, H. H. Action, time and the basal ganglia. *Philos Trans R Soc Lond B Biol Sci* **369**, 20120473,  
879 doi:10.1098/rstb.2012.0473 (2014).
- 880 63 Yin, H. H. The Basal Ganglia in Action. *Neuroscientist* **23**, 299-313, doi:10.1177/1073858416654115 (2017).
- 881 64 Granger, C. W. Investigating causal relations by econometric models and cross-spectral methods.  
882 *Econometrica: journal of the Econometric Society*, 424-438 (1969).
- 883 65 Gallistel, C. R. & Gibbon, J. Time, rate, and conditioning. *Psychol Rev* **107**, 289-344, doi:10.1037/0033-  
884 295x.107.2.289 (2000).
- 885 66 Bokadia, H., Rai, R. & Torres, E. B. Digitized ADOS: Social Interactions beyond the Limits of the Naked  
886 Eye. *J Pers Med* **10**, doi:10.3390/jpm10040159 (2020).
- 887 67 Do Carmo, M. *Differential Geometry of Curves and Surfaces*. (Prentice Hall, 1976).
- 888 68 Torres, E. B. *Objective biometric methods for the diagnosis and treatment of nervous system disorders*.  
889 (Academic Press, 2018).
- 890 69 Ghaderi, A. H. et al. Time estimation and beta segregation: An EEG study and graph theoretical  
891 approach. *PLoS One* **13**, e0195380 (2018).
- 892 70 Phinyomark, A., Thongpanja, S., Hu, H., Phukpattaranont, P. & Limsakul, C. The usefulness of mean  
893 and median frequencies in electromyography analysis. *Computational intelligence in electromyography*  
894 *analysis-A perspective on current applications and future challenges*, 195-220 (2012).
- 895 71 Wang, T., Bebbington, M. S. & Harte, D. S. A comparative study of coherence, mutual information and  
896 cross-intensity models. *International Journal of Information and Systems Sciences* **6**, 49-60 (2008).
- 897 72 Ryu, J. & Torres, E. B. Characterization of Sensory-Motor Behavior Under Cognitive Load Using a New  
898 Statistical Platform for Studies of Embodied Cognition. *Front. Hum. Neurosci.* **12**, 1-19,  
899 doi:10.3389/fnhum.2018.00116 (2018).
- 900 73 Kalampratsidou, V. & Torres, E. B. Peripheral Network Connectivity Analyses for the Real-Time  
901 Tracking of Coupled Bodies in Motion. *Sensors (Basel)* **18**, doi:10.3390/s18093117 (2018).
- 902 74 Vicente, R., Wibral, M., Lindner, M. & Pipa, G. Transfer entropy—a model-free measure of effective  
903 connectivity for the neurosciences. *Journal of computational neuroscience* **30**, 45-67 (2011).
- 904 75 Barnett, L., Barrett, A. B. & Seth, A. K. Granger causality and transfer entropy are equivalent for  
905 Gaussian variables. *Physical review letters* **103**, 238701 (2009).
- 906 76 Ding, M., Chen, Y. & Bressler, S. L. 17 Granger causality: basic theory and application to neuroscience.  
907 *Handbook of time series analysis: recent theoretical developments and applications* **437** (2006).
- 908

909 **Author Contributions:** T.B. and E.B.T. conceptualized the study, designed the methodology and  
910 wrote the software. T.B. did the validation, investigation, and formal analysis. T.B. and E.B.T.  
911 designed the figures / visualization tools. R.R. and J.R. did the data collection and curation. T.B. and  
912 E.B.T. did the original writing—original draft preparation, and all authors reviewed and edited the  
913 MS to its final state. E.B.T. did the project supervision, administration, and funding acquisition. All  
914 authors have read and agreed to the published version of the manuscript.

915 **Funding:** This research was funded by The New Jersey Governor's Council for the Medical Research  
916 and Treatments of Autism, grant number CAUT15APL038 and by the Nancy Lurie Marks Family  
917 Foundation Career Development Award to EBT.

918 **Acknowledgments:** We thank all participants in the study.

919 **Conflicts of Interest:** The authors declare no conflict of interest. The funders had no role in the design  
920 of the study; in the collection, analyses, or interpretation of data; in the writing of the manuscript, or  
921 in the decision to publish the results.

922



© 2021 by the authors. Submitted for possible open access publication under the terms and conditions of the Creative Commons Attribution (CC BY) license (<http://creativecommons.org/licenses/by/4.0/>).

923

# Figures

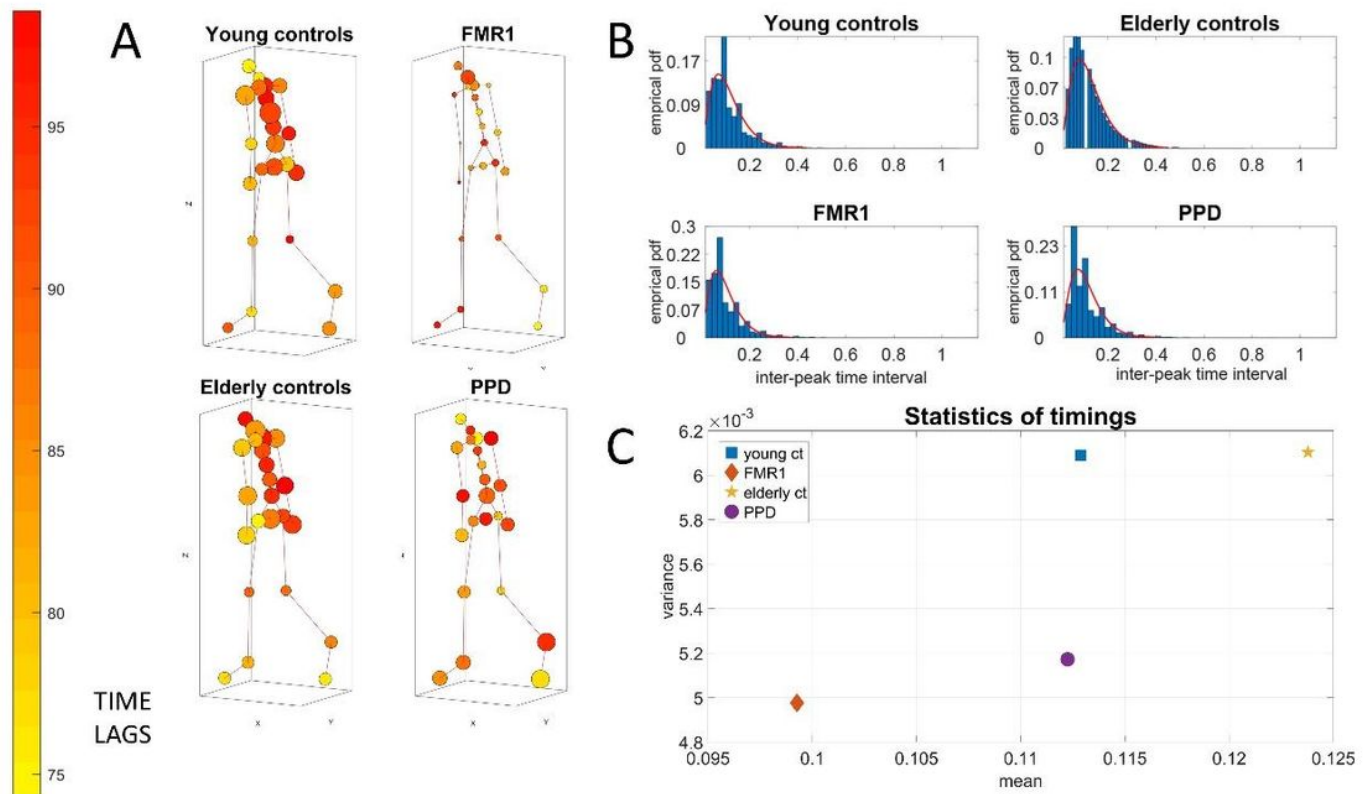


**Figure 1**

GC Optimal Lag Maps and timing information. Anthropomorphic network representation of human walking patterns. The nodes' size is proportional to the number of outgoing links connected to the other nodes in the network (out degree) of the average GC network. The color of the nodes is the maximum optimal lag response of a node with the rest of the body for the average Lag Response network. A unit of one lag refers to the distance in time between two peaks. The actual physical time between the two peaks can vary. The frequency histograms depict the distribution of the inter-peak timings for each group. The empirical distributions are well fitted by the gamma family of distributions. For the young controls, the average inter-peak timing is 0.1129 seconds with a std of 0.0780. For the elderly controls, 0.1238 with a std of 0.0781. For the FMR1 carriers, 0.0993 with a std of 0.0705. For the PPDs, 0.1122 with a std of 0.0719.

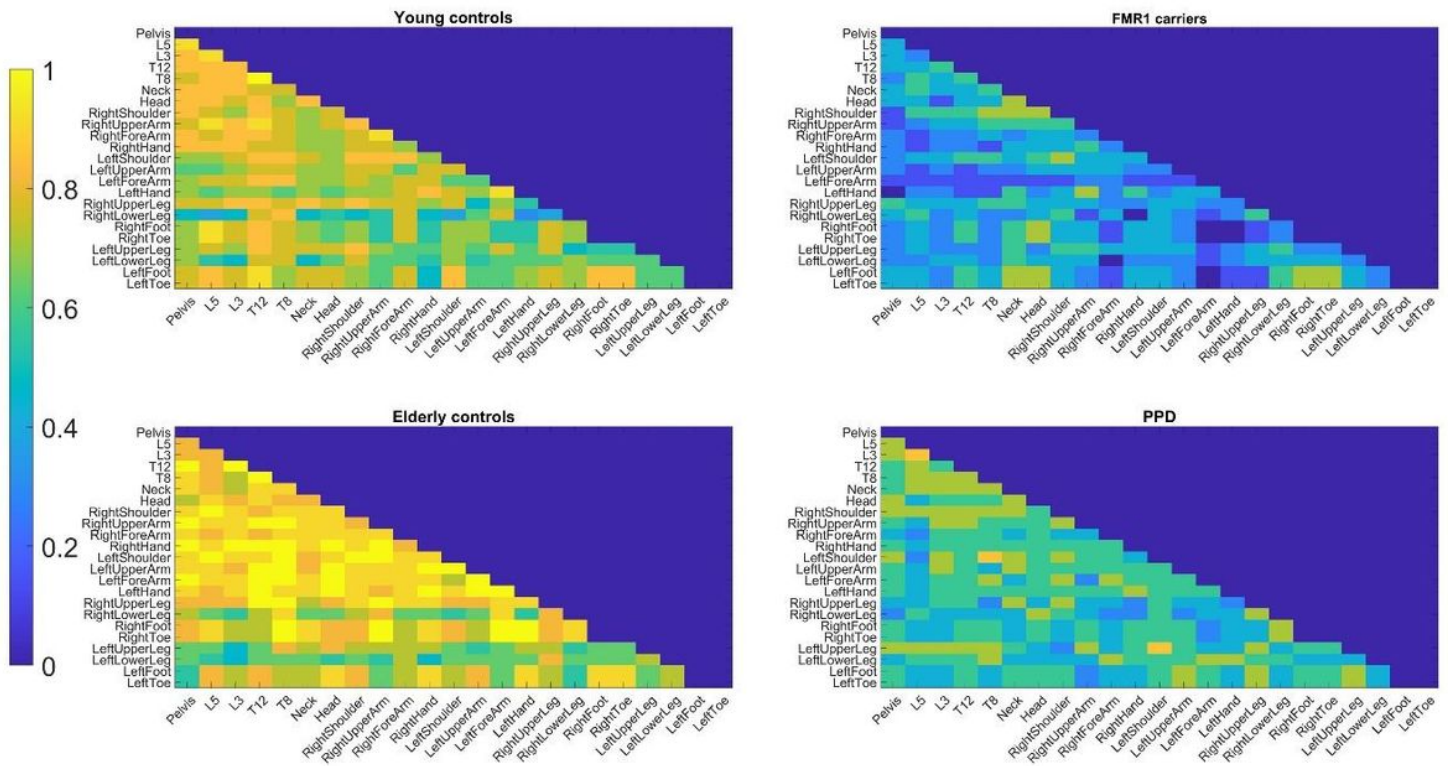
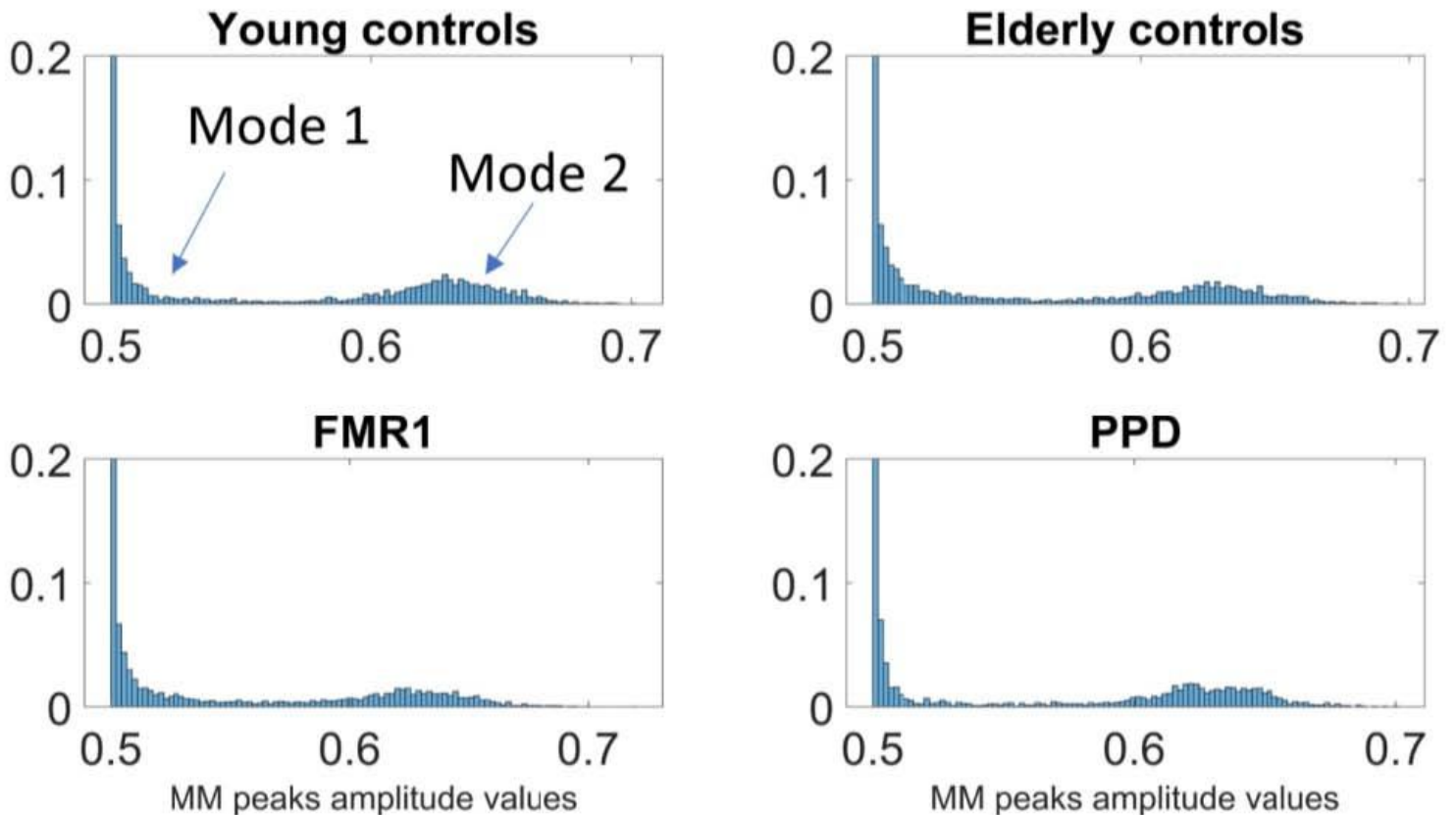


Figure 2

Feedback loops differ across groups. For each group, the figures show the percentage of subjects within the group for whom a feedback loop was detected between each pair of body nodes.



**Figure 3**

Non-unimodal distributions of MMS from peak angular speed amplitudes differentiate groups. Different modes are specific to each cohort, mode 1 exponential and mode 2 Gaussian, with different dispersions and percentages of points in each mode.

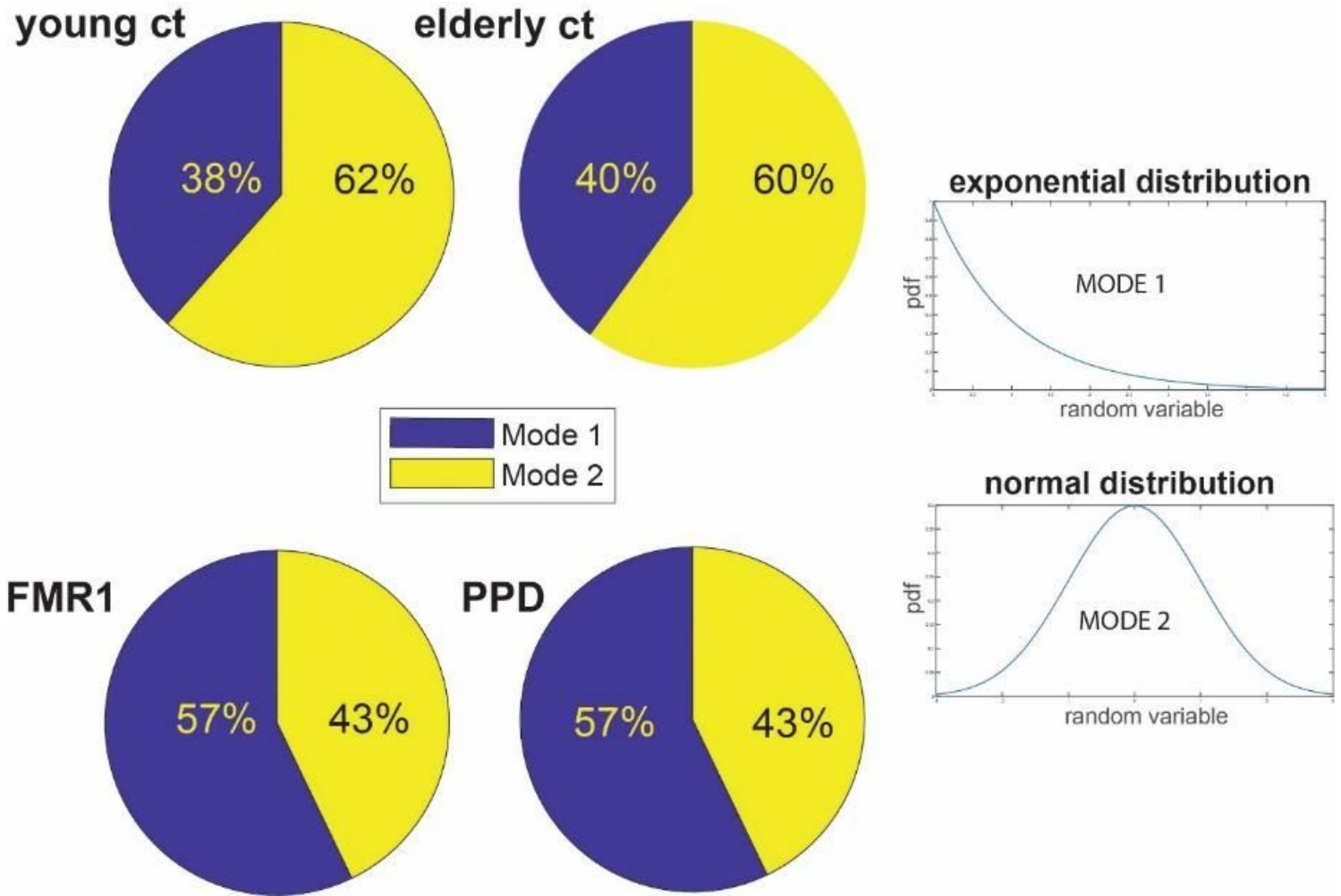


**Figure 4**

Percentages of distribution's modes varies across groups with lowest Exponential mode in young controls and highest in FMR1 carriers and PPD. Gaussian mode is highest in young controls and elderly controls and comparable between PPD (higher) and FMR1-carriers.

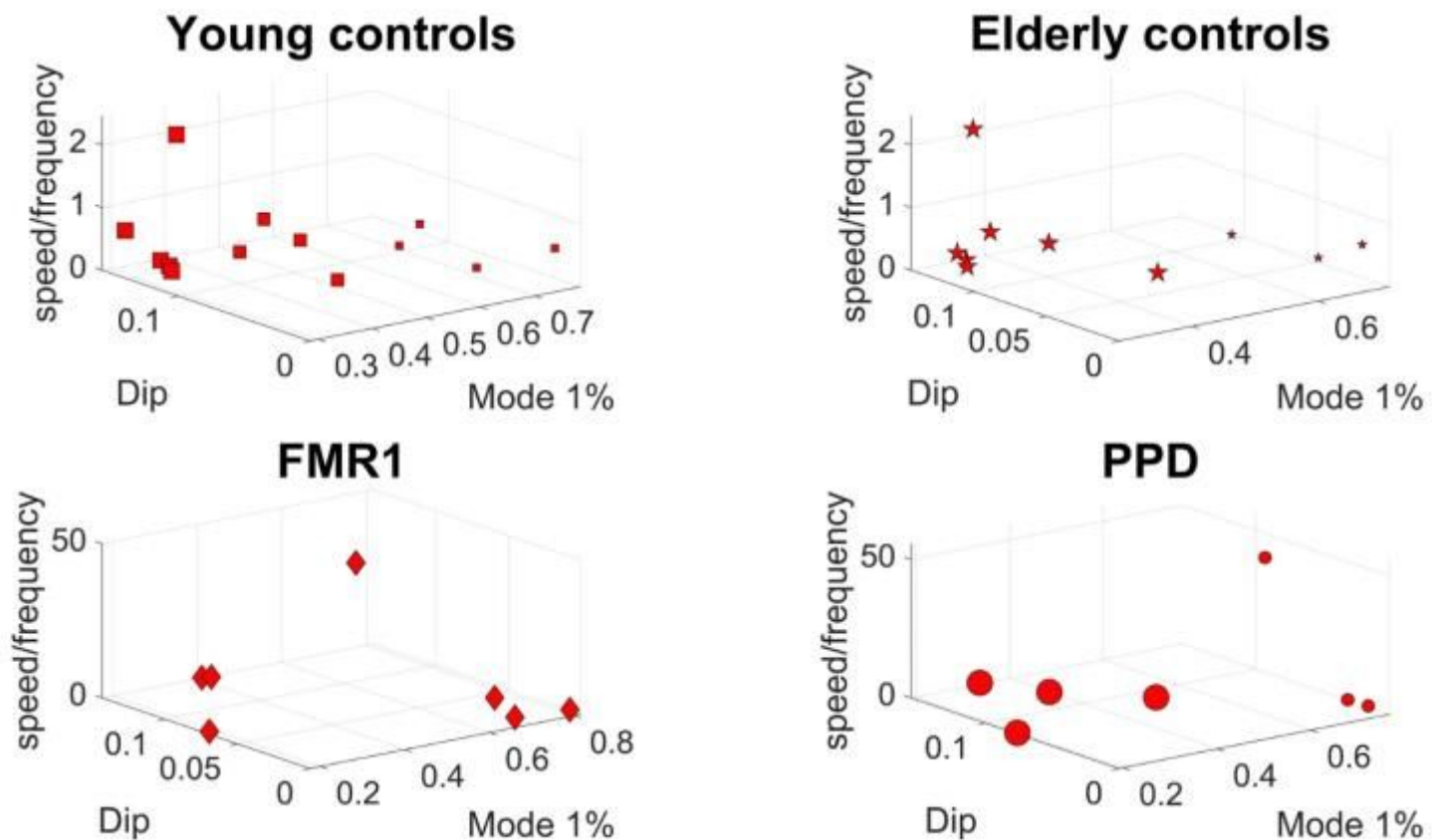


**Figure 5**

Subgroups within each group revealed by group's clusters. The clusters for each group using the k-means clustering algorithm with 3 for young controls and 2 for each of the other groups. Subtypes of activity emerge for all groups. The empirical distributions for the MMS of the norm of the lower body COM 3D position data series for the 4 groups are bimodal for all 4 groups.

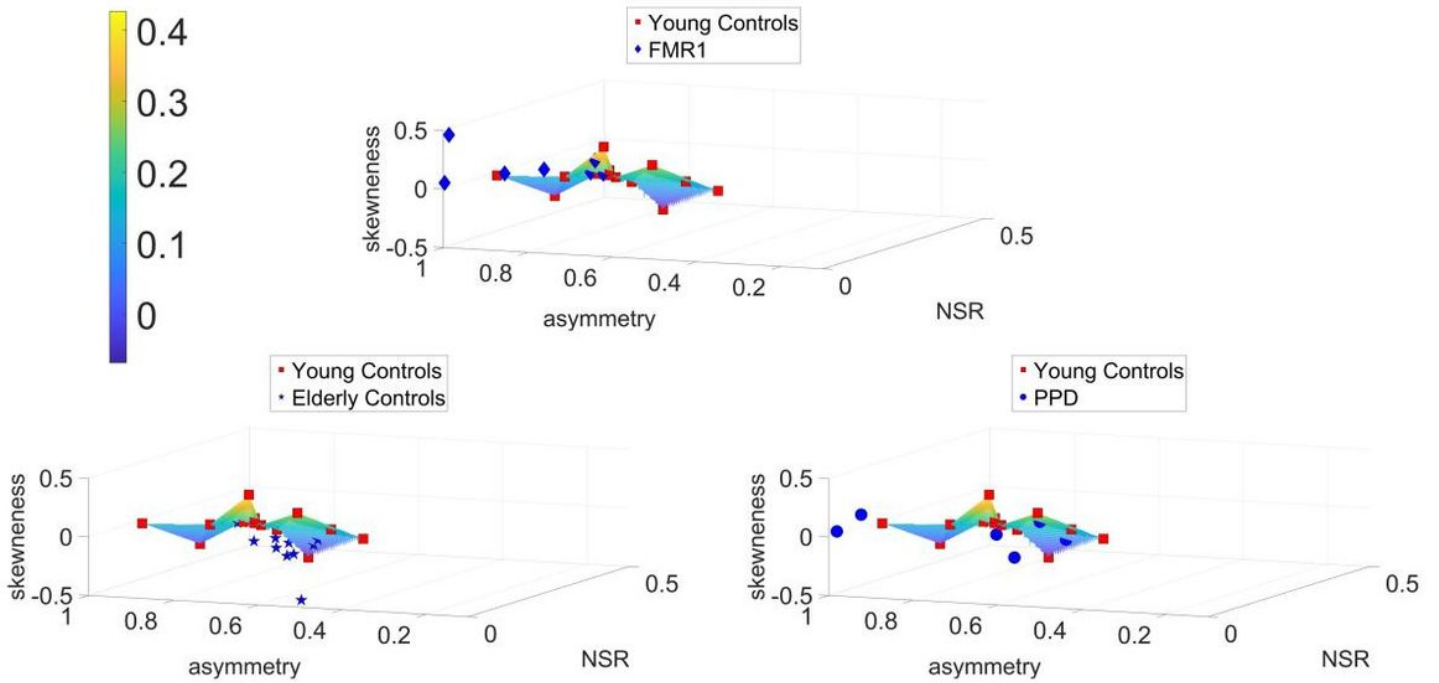


**Figure 6**

Parameter space reveal differences across groups. NSR, GC network asymmetry and average Skewness are used to build a parameter space showing departure from young controls scatter fitted by a surface. Scatters from the FMR1 carriers, the elderly controls and the PPD largely depart from young controls' surface. Color bar reflects skewness range of values.

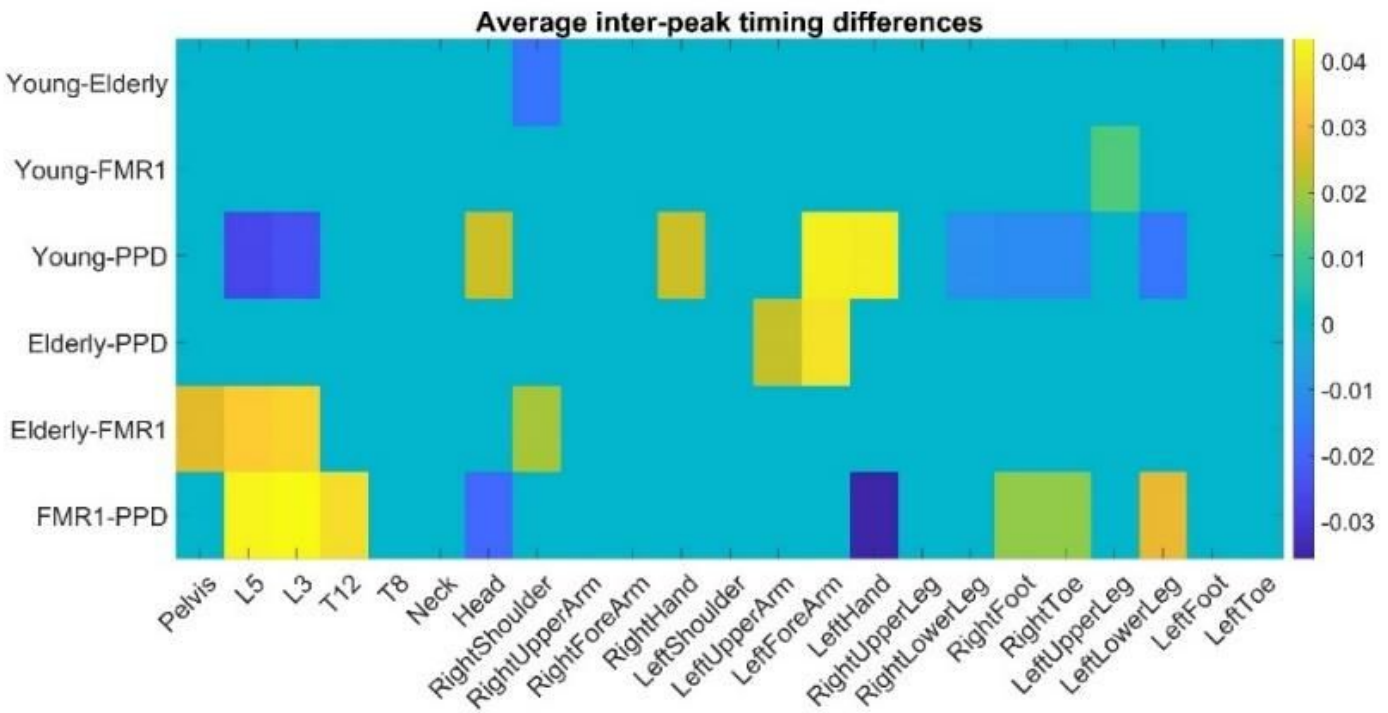


**Figure 7**

The average differences in inter-peak timings (seconds) taken for each group across all nodes, reveal separation between groups. A difference of zero (cyan color) indicates no significant difference ( $p=0.05$ ).

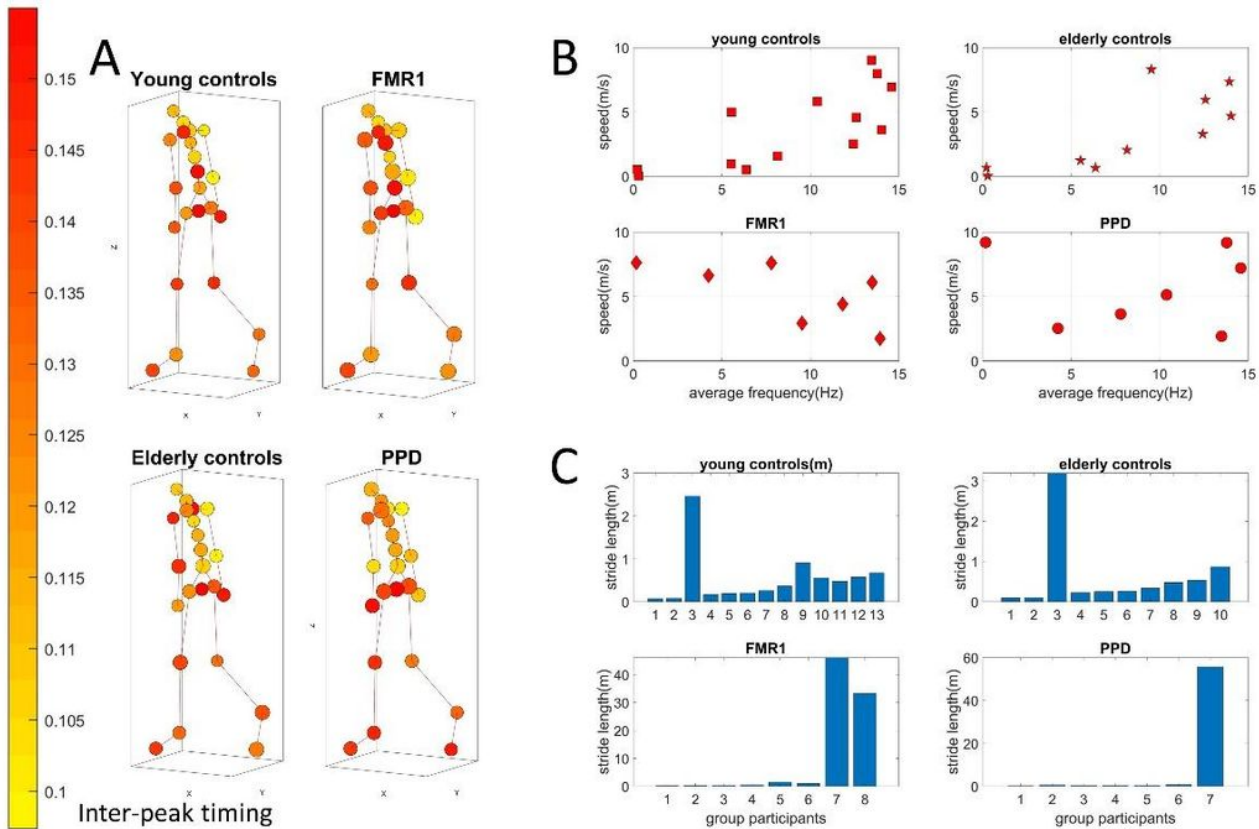


**Figure 8**

Stride-length differences from speed to frequency ratio obtained from the center of mass trajectories, separate healthy aging from nervous systems disorders. (A) Network representation in anthropomorphic avatar form. The size of the nodes is proportional to the maximum coupling frequency (the one that maximizes cross-coherence) of a node with the rest of the body and the color of the nodes is the average time distance (s) between two MMS peaks. (B) Parameter space comparing speed vs. frequency. Focusing on the trajectory of the center of mass of the lower body, mean speed over mean frequency of the speed time series has a positive upward trend for healthy controls. This contrasts to a negative trend in FMR1-carriers and variable trends in PPD. (C) Both types of trends and variations span a range of values across both dimensions with stride length periodically accumulated differing across groups.

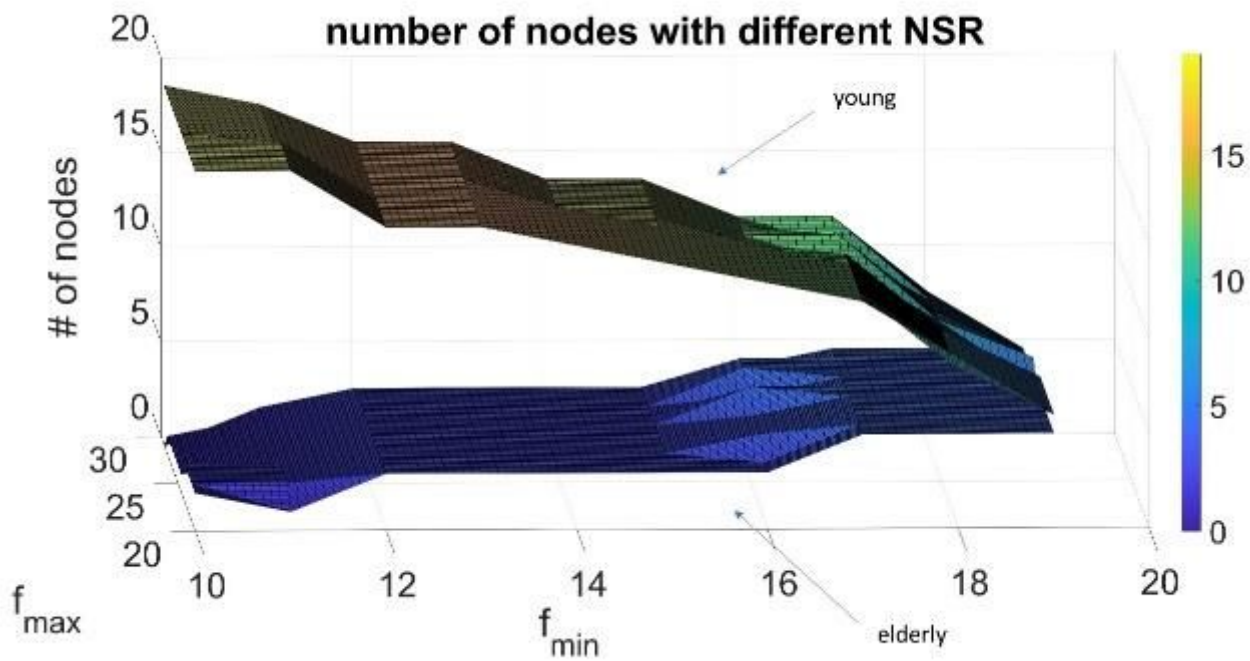


**Figure 9**

Noise cancellation by systematic frequency removal in young vs. elderly participants. The two surface plots show how after removing a component of tremor from the PPD by using band stop filtering of the angular velocity for different choices of frequency, the resulting body node networks is comparable to the NSR dimension of the young and elderly controls groups. The color bar reflects the number of nodes with different NSR that results from the noise cancellation.

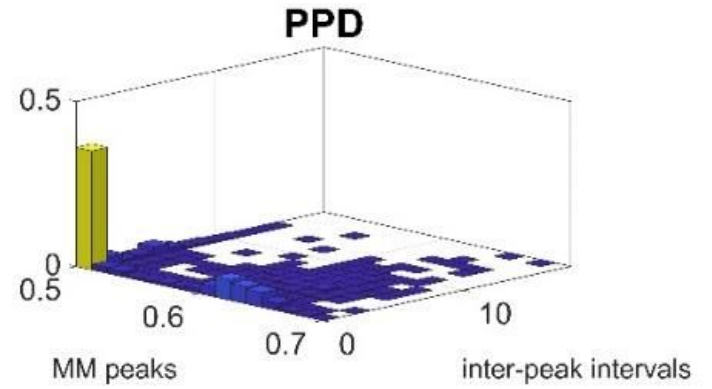
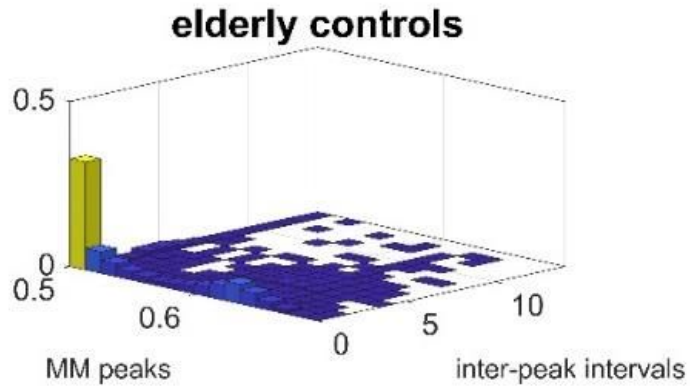
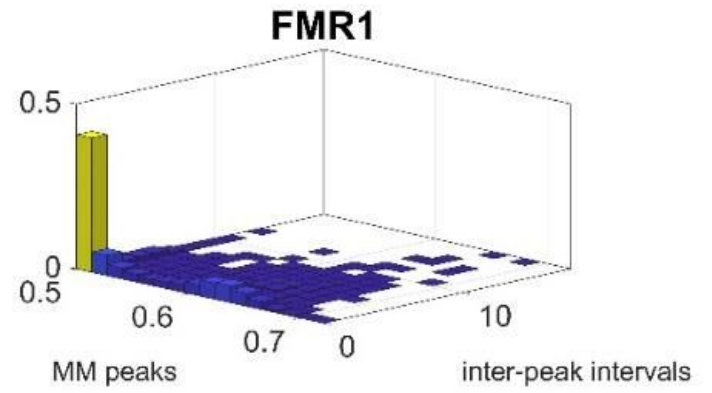
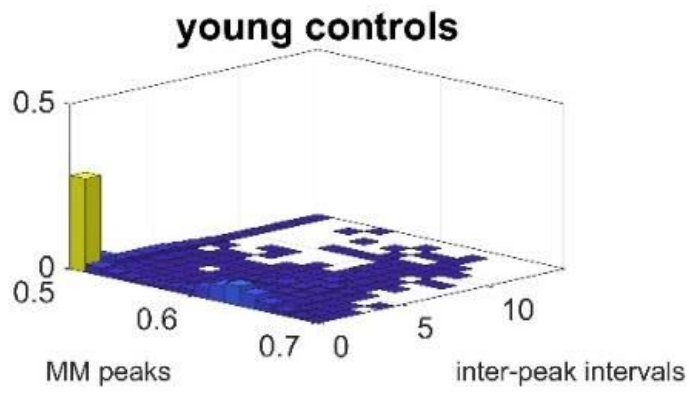


**Figure 10**

Joint empirical distribution of MMS peak values and inter-peak-interval times.

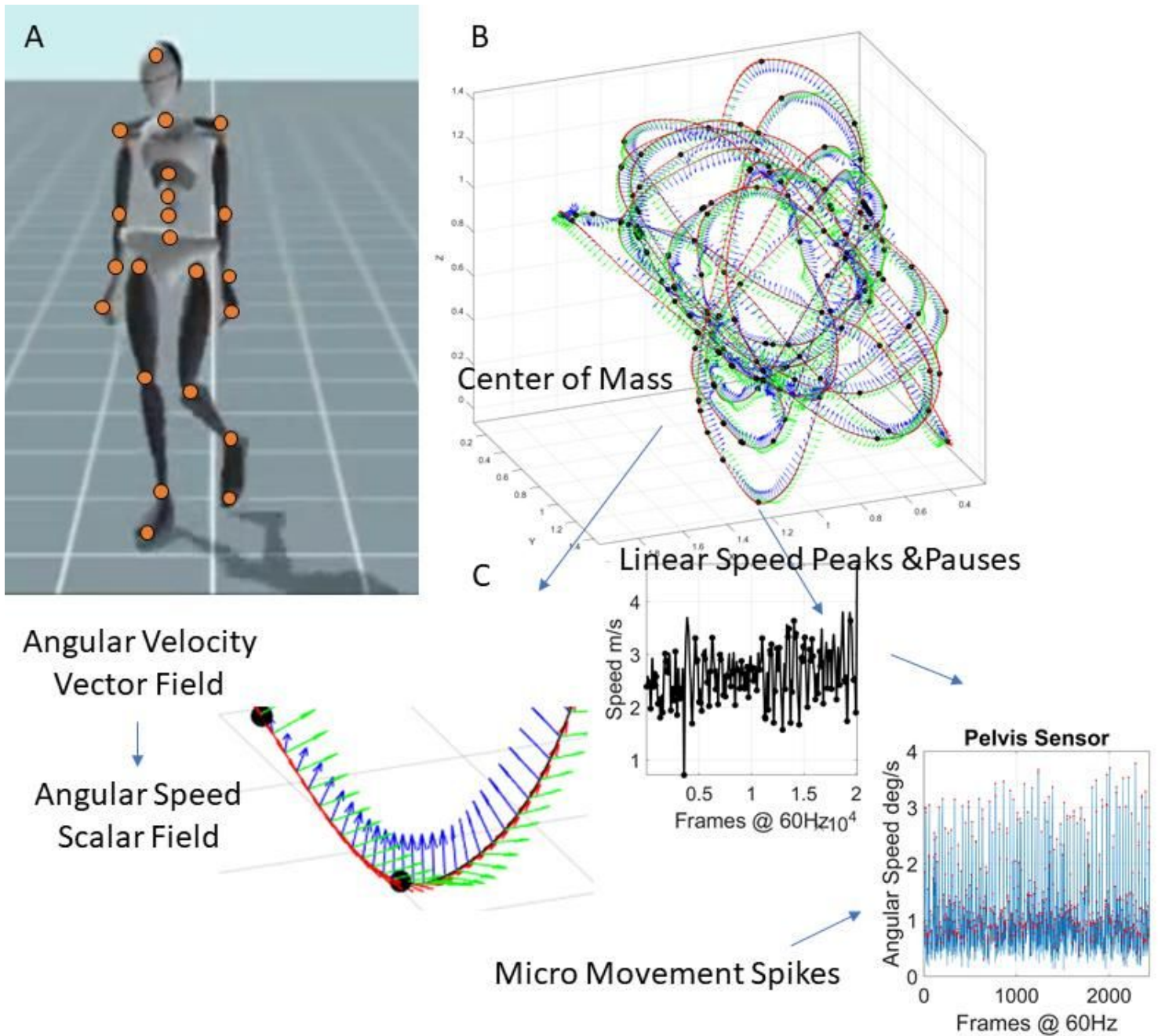


**Figure 11**

Methods Figure. (A) Data acquisition using a grid of wearable sensors calibrating position and orientation in real time and sampling changes of position in time, at 60Hz. (B) Center of Mass trajectories (m) in 3D parameterized using the Frenet-Serret frame to study geometric aspects of the curve. (C) Linear speed used to mark pauses and peaks along the curve, thus allowing us to express behavioral landmarks along other kinematics parameters such as the angular speed quantifying bodily rates of 23 joints' rotations. The MMS are derived from the fluctuations in angular speed amplitude. Red dots mark peaks (transitions of speed slope from positive to negative.)

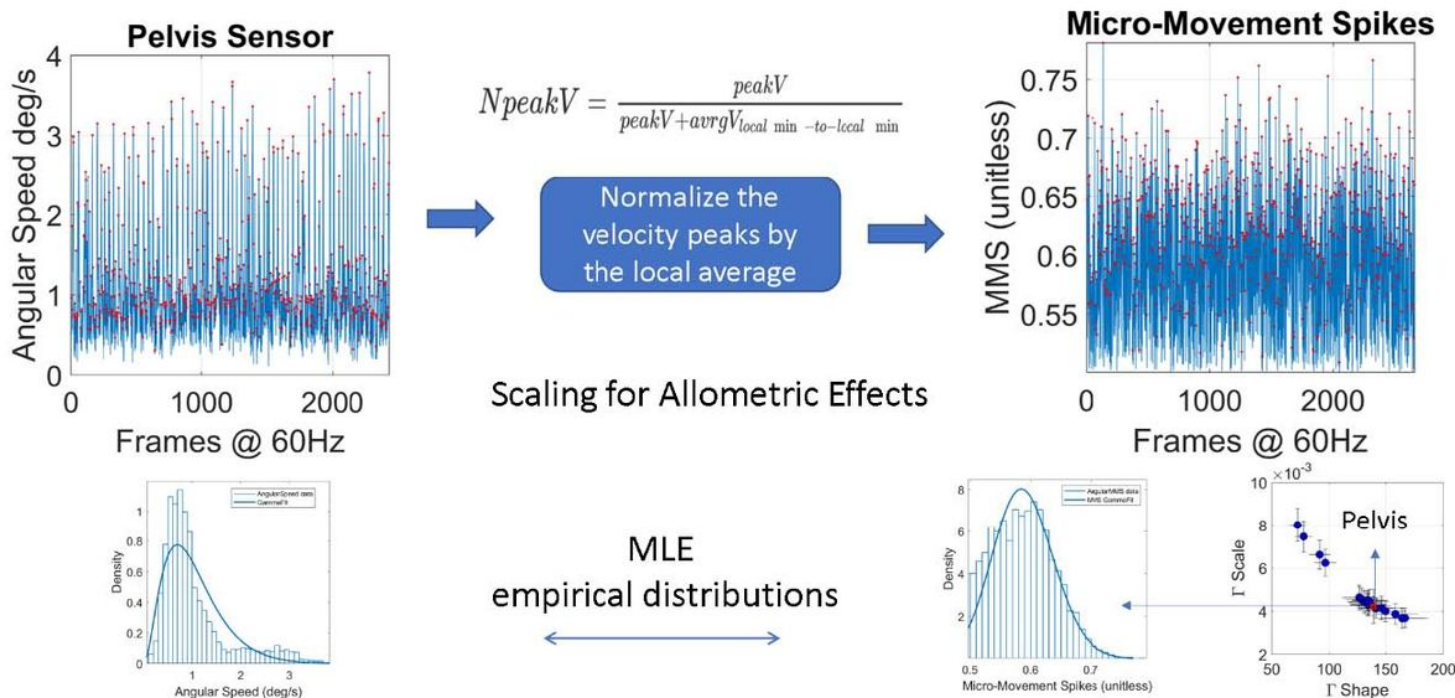


**Figure 12**

The MMS time series extraction from the angular speed tracking stochastic trajectories from all joints (red dot marks the pelvis for instance.)

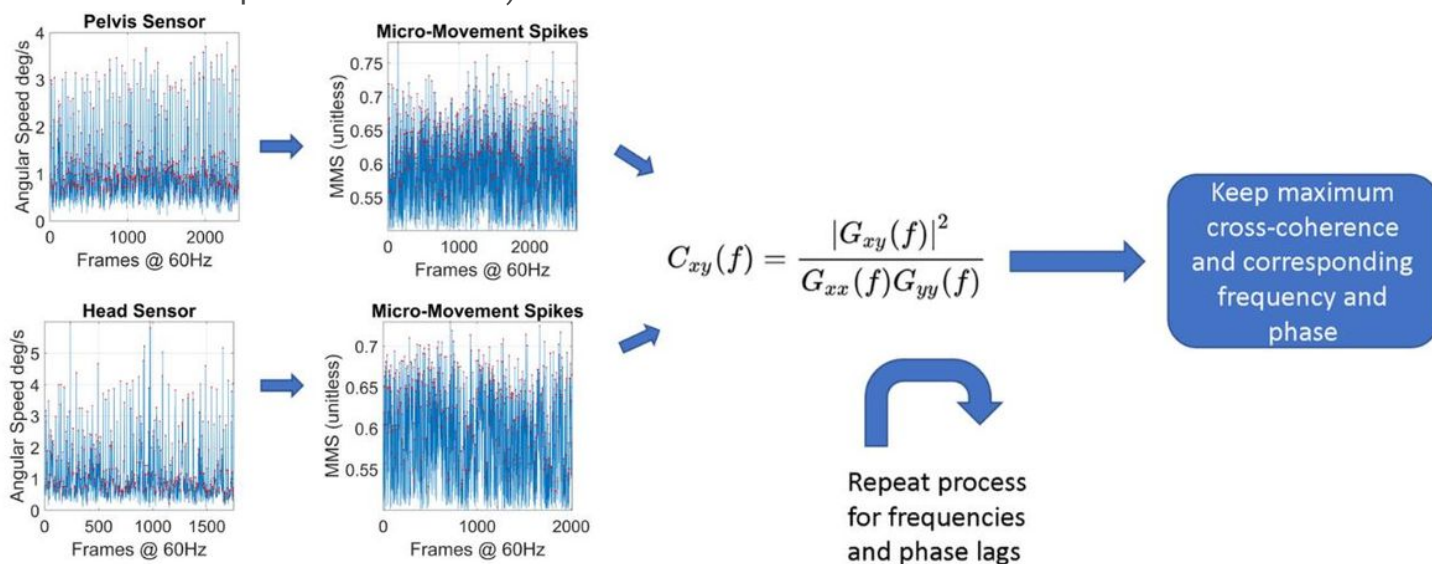


**Figure 13**

The pipeline for the calculation of the maximum cross-coherence and the frequency for which it is maximized.

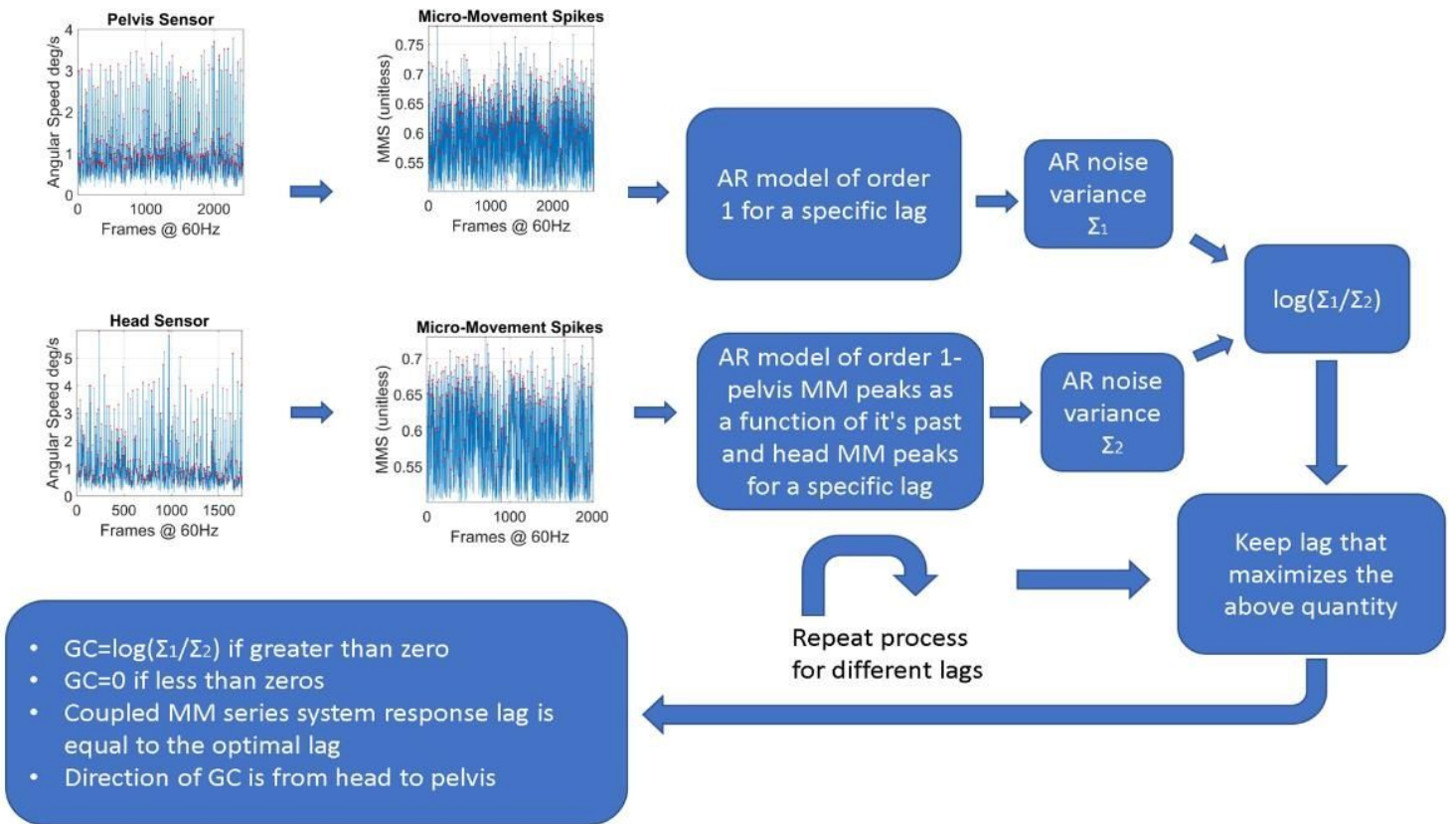


Figure 14

Pipeline for the estimation of the Granger Causality and Response time values between two body parts.